

# Evidence for Neutrino Oscillations from the Observation of $\bar{\nu}_e$ Appearance in a $\bar{\nu}_\mu$ Beam

A. Aguilar,<sup>5</sup> L.B. Auerbach,<sup>8</sup> R.L. Burman,<sup>5</sup> D.O. Caldwell,<sup>3</sup> E.D. Church,<sup>1</sup>  
A.K. Cochran,<sup>7\*</sup> J.B. Donahue,<sup>5</sup> A. Fazely,<sup>7</sup> G.T. Garvey,<sup>5</sup> R.M. Gunasingha,<sup>7</sup>  
R. Imlay,<sup>6</sup> W. C. Louis,<sup>5</sup> R. Majkic,<sup>8</sup> A. Malik,<sup>6</sup> W. Metcalf,<sup>6</sup> G.B. Mills,<sup>5</sup>  
V. Sandberg,<sup>5</sup> D. Smith,<sup>4</sup> I. Stancu,<sup>1†</sup> M. Sung,<sup>6</sup> R. Tayloe,<sup>5‡</sup>  
G.J. VanDalen,<sup>1</sup> W. Vernon,<sup>2</sup> N. Wadia,<sup>6</sup> D.H. White,<sup>5</sup> S. Yellin<sup>3</sup>

(LSND Collaboration)

<sup>1</sup> *University of California, Riverside, CA 92521*

<sup>2</sup> *University of California, San Diego, CA 92093*

<sup>3</sup> *University of California, Santa Barbara, CA 93106*

<sup>4</sup> *Embry Riddle Aeronautical University, Prescott, AZ 86301*

<sup>5</sup> *Los Alamos National Laboratory, Los Alamos, NM 87545*

<sup>6</sup> *Louisiana State University, Baton Rouge, LA 70803*

<sup>7</sup> *Southern University, Baton Rouge, LA 70813 and*

<sup>8</sup> *Temple University, Philadelphia, PA 19122*

(Dated: November 26, 2024)

---

<sup>\*</sup> now at New Brunswick Laboratory, Argonne, IL 60439

<sup>†</sup> now at University of Alabama, Tuscaloosa, AL 35487

<sup>‡</sup> now at Indiana University, Bloomington, IN 47405

## Abstract

A search for  $\bar{\nu}_\mu \rightarrow \bar{\nu}_e$  oscillations was conducted by the Liquid Scintillator Neutrino Detector at the Los Alamos Neutron Science Center using  $\bar{\nu}_\mu$  from  $\mu^+$  decay at rest. A total excess of  $87.9 \pm 22.4 \pm 6.0$  events consistent with  $\bar{\nu}_e p \rightarrow e^+ n$  scattering was observed above the expected background. This excess corresponds to an oscillation probability of  $(0.264 \pm 0.067 \pm 0.045)\%$ , which is consistent with an earlier analysis. In conjunction with other known limits on neutrino oscillations, the LSND data suggest that neutrino oscillations occur in the  $0.2 - 10 \text{ eV}^2/c^4 \Delta m^2$  range, indicating a neutrino mass greater than  $0.4 \text{ eV}/c^2$ .

## I. INTRODUCTION

A neutrino produced in a weak decay is always from a specific family,  $\nu_e$ ,  $\nu_\mu$ , or  $\nu_\tau$ , that is directly associated with the charged lepton accompanying the decay. When this neutrino is detected in a charged-current reaction, it manifests its identity by transforming into the anti-particle of the charged lepton that accompanied its creation. Lepton family number is then conserved. However, the result is different if the neutrino changes from one family to another. For example, if a  $\nu_\mu$  changes to a  $\nu_e$ , then a  $\mu^+$  is made at the neutrino's creation and an  $e^-$  created at its demise, in clear violation of lepton family number. Such neutrino oscillations are viewed as possible, or even likely, as the flavor eigenstates ( $\nu_e$ ,  $\nu_\mu$ ,  $\nu_\tau$ ) need not be neutrino mass eigenstates ( $\nu_1$ ,  $\nu_2$ ,  $\nu_3$ ). If the neutrino flavor eigenstates are a linear combination of the mass eigenstates, the neutrino flavor must change with time because the phases of the mass eigenstates evolve at different rates. In the case of two flavor eigenstates ( $\nu_a$ ,  $\nu_b$ ), the probability that  $\nu_a$  will turn into  $\nu_b$  is given by

$$P(ab) = \sin^2(2\theta) \sin^2\left(1.27\Delta m^2 \frac{L_\nu}{E_\nu}\right), \quad (1.1)$$

where  $\theta$  is the mixing angle between the mass eigenstates  $\nu_1$  and  $\nu_2$ ,  $\Delta m^2$  is the difference in neutrino eigenstate masses squared,  $m_1^2 - m_2^2$ , in  $\text{eV}^2/c^4$ ,  $L_\nu$  is the distance traveled by the neutrino in meters, and  $E_\nu$  the neutrino energy in MeV.

A search for neutrino oscillations requires knowledge of the neutrino source, both with respect to the flavor composition and energy spectrum of the source. There are two types of searches. The first seeks to observe a reduction in the expected number of detected neutrinos of a specific flavor. Characterizing the reduction as  $P(aa) = 1 - P(ab)$ , it can then be explained in terms of neutrino oscillations. Such searches are termed *disappearance* experiments. The second method looks for a greater than expected number of events ascribed to a neutrino flavor that is either absent or very weakly produced at the neutrino source. These searches are referred to as *appearance* measurements. The results of the search reported in this paper are of the latter kind. It reports an excess of events ascribed to electron antineutrinos that is approximately five times greater than the number of such events believed to be created at the neutrino source.

Neutrinos are assumed to be massless in the Standard Model, so the observation of neutrino oscillations would require an extension of the current version. In addition, as there are  $\sim 100$  neutrinos per  $\text{cm}^3$  of each neutrino family left over from the initial expansion

of the universe, neutrino masses of even a few  $\text{eV}/c^2$  would have a significant effect on the evolving structure of the universe.

The source of neutrinos for the measurement in this report is the interaction of the intense ( $\sim 1$  mA) 798 MeV proton beam at the Los Alamos Neutron Science Center (LANSCE), which produces a large number of pions, mostly  $\pi^+$ . The  $\pi^-$  are mainly absorbed and only a small fraction decay to  $\mu^-$ , which in turn are largely captured. Thus, the resulting neutrino source is dominantly due to  $\pi^+ \rightarrow \mu^+ \nu_\mu$  and  $\mu^+ \rightarrow e^+ \nu_e \bar{\nu}_\mu$  decays, most of which decay at rest (DAR). Such a source has a paucity of  $\bar{\nu}_e$ , and so measurement of the reaction  $\bar{\nu}_e p \rightarrow e^+ n$ , which has a large and well known cross section, provides a sensitive way to search for  $\bar{\nu}_\mu \rightarrow \bar{\nu}_e$  oscillations. Such events are identified by detection of both the  $e^+$  and the 2.2 MeV  $\gamma$  from the reaction  $np \rightarrow d\gamma$ . In addition, the  $\nu_e$  flux from  $\pi^+$  and  $\mu^+$  decay-in-flight (DIF) is very small, which allows a search for  $\nu_\mu \rightarrow \nu_e$  oscillations via the measurement of electrons above the Michel electron endpoint from the reaction  $\nu_e C \rightarrow e^- N$ .

The Liquid Scintillation Neutrino Detector (LSND) experiment took data over six calendar years (1993-1998). During this period the LANSCE accelerator operated for 17 months, delivering 28,896 C of protons on the production target. Using partial samples of the resulting data, evidence for neutrino oscillations has been published previously [1, 2, 3]. This report presents the final results on oscillations using all the data, combining the  $\bar{\nu}_\mu \rightarrow \bar{\nu}_e$  and  $\nu_\mu \rightarrow \nu_e$  searches into a single analysis with common selection criteria, and employing a new event reconstruction that greatly improves the spatial resolution. An excess of events consistent with neutrino oscillations is observed which requires that at least one neutrino have a mass greater than  $0.4 \text{ eV}/c^2$ .

Neutrino oscillations have also been employed to explain the observed deficit of solar neutrinos [4] and the atmospheric neutrino anomaly [5] by  $\nu_e$  and  $\nu_\mu$  disappearance, respectively. The Super Kamiokande atmospheric results [6] favor  $\nu_\mu \rightarrow \nu_\tau$  and provide compelling evidence for neutrino oscillations. It is difficult to explain the solar neutrino deficit, the atmospheric neutrino anomaly, and the LSND excess of events with only three flavors of neutrinos, so that a fourth, sterile neutrino has been proposed to explain all of the data [7]. Neutrino oscillations between active and sterile neutrinos could have a significant effect on the R process in type II supernovae [8].

## II. NEUTRINO BEAM, DETECTOR, AND DATA COLLECTION

### A. Proton Beam and Targets

The LSND experiment [9] was designed to search for  $\bar{\nu}_\mu \rightarrow \bar{\nu}_e$  oscillations from  $\mu^+$  DAR with high sensitivity. A layout of the detector and beam stop is shown in Fig. 1. The LANSCE accelerator is an intense source of low energy neutrinos produced with a proton current of 1 mA at 798 MeV kinetic energy. For the 1993-1995 running period the production target consisted of a 30-cm long water target (20-cm in 1993) followed by a water-cooled Cu beam dump, while for the 1996-1998 running period the production target was reconfigured with the water target replaced by a close-packed, high-Z target. The muon DAR neutrino flux with the latter configuration was only 2/3 of the neutrino flux with the original water target, while the pion DIF neutrino flux was reduced to 1/2 of the original flux. The resulting DAR neutrino fluxes are well understood because almost all detectable neutrinos arise from  $\pi^+$  or  $\mu^+$  decay;  $\pi^-$  and  $\mu^-$  that stop are readily captured in the Fe of the shielding and Cu of the beam stop [10]. The production of kaons or heavier mesons is negligible at these proton energies. The  $\bar{\nu}_e$  flux is calculated to be only  $\sim 8 \times 10^{-4}$  as large as the  $\bar{\nu}_\mu$  flux in the  $20 < E_\nu < 52.8$  MeV energy range, so that the observation of a  $\bar{\nu}_e$  event rate significantly above the calculated background would be evidence for  $\bar{\nu}_\mu \rightarrow \bar{\nu}_e$  oscillations.

For the first three years of data taking, thin carbon targets were in place in positions A1 and A2 at the experimental area of the LANSCE accelerator, but dominant pion production occurred at the A6 beam stop, which accounted for  $\sim 98\%$  of the DAR neutrino flux and  $\sim 95\%$  of the DIF neutrino flux. The A1, A2, and A6 targets were approximately 135 m, 110 m, and 30 m, respectively, from the center of the LSND detector. A6 was essentially the only source of neutrinos for the last three years of data taking. Note that in each case there was a small open space downstream of the primary targets where a few percent of the pions decay in flight, producing  $\nu_\mu$  up to an energy of 300 MeV. The neutrino flux was calculated by a program [10] using particle production data for thin targets taken at a number of proton energies and extrapolated to the actual geometry represented. Fig. 2 shows the layout of the A6 beam stop as it was configured for the 1993-1995 data taking. Table I shows the proton beam statistics for each of the six years of running from 1993 through 1998.

## B. Neutrino Sources

Neutrinos arise from both pion and muon decays. The pion decay modes are  $\pi^+ \rightarrow \mu^+ \nu_\mu$ ,  $\pi^+ \rightarrow e^+ \nu_e$ ,  $\pi^- \rightarrow \mu^- \bar{\nu}_\mu$ , and  $\pi^- \rightarrow e^- \bar{\nu}_e$ . The  $\pi^+$  decay occurs both with the pion at rest (97%) and in flight (3%). The  $\pi^-$ , however, only decays in flight as they are totally absorbed on nuclei when they stop. Helium represents an anomalous case in which  $\pi^-$  decay occurs occasionally, but this effect is negligible in other nuclei [11]. Muon decay modes are  $\mu^+ \rightarrow e^+ \nu_e \bar{\nu}_\mu$  and  $\mu^- \rightarrow e^- \bar{\nu}_e \nu_\mu$ . Almost all  $\mu^+$  stop before decaying and produce a normal Michel spectrum for  $\nu_e$  and  $\bar{\nu}_\mu$ . The  $\mu^-$  are produced following  $\pi^-$  DIF and either decay in orbit or are absorbed in a nucleus through  $\mu^- N \rightarrow \nu_\mu X$ , where  $E_\nu < 90$  MeV. The absorption rates are taken from [12] and are shown in Table II. Each of these production processes has been included in the flux calculation described below.

## C. Production Monte Carlo

The Production Monte Carlo [10] simulates the decays of pions and muons for each of the decay and absorption reactions described above and for each of the configurations listed in Table I. Pion production data using a number of different proton energies were input, as well as information on the target materials. The particles were tracked through the specified materials and geometries. For each configuration, the flux and energy spectrum of neutrinos from each decay channel were obtained for 25 different positions within the detector. For DAR neutrinos the flux is isotropic. The accumulated charge of beam protons was used to obtain the number of protons on target, and for each year of running the resulting fluxes and spectra from all configurations were added together, weighted by the accumulated beam charges. The program gives fluxes in terms of the number of neutrinos traversing the detector region per proton on target per unit of area.

## D. Neutrino Fluxes

Fig. 3 shows the neutrino energy spectra from the largest DAR sources. The  $\bar{\nu}_\mu$  flux from  $\mu^+$  DAR provides the neutrinos for the  $\bar{\nu}_\mu \rightarrow \bar{\nu}_e$  oscillation analysis. The  $\nu_e$  flux from  $\mu^+$  DAR provides events used to verify the DAR neutrino fluxes, as discussed later in this paper. The  $\bar{\nu}_e$  flux from  $\mu^-$  DAR is a background to the oscillation signal with an energy

spectrum similar to that of  $\nu_e$  from  $\mu^+$  decay.

Fig. 4 shows the neutrino energy spectra from various DIF sources averaged over the detector. The  $\nu_\mu$  flux from  $\pi^+$  DIF provides neutrinos for the  $\nu_\mu \rightarrow \nu_e$  oscillation analysis. The  $\nu_e$  flux from  $\mu^+$  and  $\pi^+$  DIF is a background for the DIF oscillation analysis. The  $\mu^+$  DIF flux is suppressed due to the long muon lifetime, while the  $\pi^+$  DIF flux is suppressed due to the small  $\pi^+ \rightarrow e^+\nu_e$  branching ratio of  $1.2 \times 10^{-4}$ .

Calculations of  $\mu^+$  DAR fluxes are uncertain at the 7% level, while  $\pi^\pm$  DIF fluxes and  $\mu^-$  DAR fluxes are uncertain to 15% [9]. Neutrino fluxes for different years are shown in Table III.

### E. Detector

The LSND detector [9] consisted of an approximately cylindrical tank 8.3 m long by 5.7 m in diameter. The center of the detector was 30 m from the A6 neutrino source. On the inside surface of the tank, 1220 8-inch Hamamatsu phototubes (PMTs) covered 25% of the area with photocathode. The tank was filled with 167 metric tons of liquid scintillator consisting of mineral oil and 0.031 g/l of b-PBD. This low scintillator concentration allows the detection of both Čerenkov light and scintillation light and yields an attenuation length of more than 20 m for wavelengths greater than 400 nm [13]. A typical 45 MeV electron created in the detector produced a total of  $\sim 1500$  photoelectrons, of which  $\sim 280$  photoelectrons were in the Čerenkov cone. PMT time and pulse-height signals were used to reconstruct the track with an average RMS position resolution of  $\sim 14$  cm, an angular resolution of  $\sim 12$  degrees, and an energy resolution of  $\sim 7\%$  at the Michel endpoint of 52.8 MeV. The Čerenkov cone for relativistic particles and the time distribution of the light, which is broader for non-relativistic particles [9], gave excellent separation between electrons and particles below Čerenkov threshold.

Cosmic rays were attenuated by roughly 2 kg/cm<sup>2</sup> of overburden. The cosmic ray trigger rate was then reduced from around 10 kHz to an acceptable level of roughly 50 Hz by an active veto shield. The veto shield enclosed the detector on all sides except the bottom, as shown in Fig. 1 by the heavy black line surrounding the detector. The main veto shield [14] consisted of a 15-cm layer of liquid scintillator in an external tank and 15 cm of lead shot in an internal tank. Following the 1993 running, additional counters were placed over

the crack between the endcap veto and the barrel region veto system, and below the veto shield along the sides. That reduced cosmic-ray background entering through veto shield gaps and the bottom support structure. The combination of active and passive shielding tagged cosmic-ray muons that stopped in the lead shot. A veto inefficiency  $< 10^{-5}$  was achieved for incident charged particles.

## F. Data Acquisition

Digitized time and pulse height of each of the 1220 detector PMTs (and each of the 292 veto shield PMTs) were recorded when the deposited energy in the tank exceeded a threshold of 150 hit PMTs ( $\sim 4$  MeV electron-equivalent energy) with  $< 4$  veto PMT hits and with no event with  $> 5$  veto PMT hits within the previous  $15.2 \mu\text{s}$ . Activity in the detector or veto shield during the  $51.2 \mu\text{s}$  preceding a primary trigger was also recorded, provided there were  $> 17$  detector PMT hits or  $> 5$  veto PMT hits. Data were recorded for 1 ms after the primary trigger at a reduced threshold of 21 PMT hits (about 0.7 MeV) in order to detect the 2.2 MeV  $\gamma$  from neutron capture on free protons, which has a capture time of  $186 \mu\text{s}$ . The detector events were recorded without reference to the beam spill, but the state of the beam was recorded with the event. Approximately 94% of the recorded events occurred between beam spills, which allowed an accurate measurement and subtraction of cosmic-ray background surviving the event selection criteria.

As most muons from muon-neutrino induced events do not satisfy the PMT trigger threshold, these muons were typically past events, while the electrons from their decay were the primary events. In contrast, electrons from electron-neutrino induced events were usually primary events. Future events include neutron capture  $\gamma$ s and  $\beta$ -decay electrons and positrons. Identification of neutrons was accomplished through the detection of the 2.2 MeV  $\gamma$  from neutron capture on a free proton. Nitrogen and boron ground-state  $\beta$ -decays occurred after the primary events with longer lifetimes of 16 and 30 ms, respectively. A given primary event can have many associated past events and future events.



### III. NEUTRINO INTERACTIONS AND EVENT SIMULATION

The neutrino interactions that occurred in LSND came from interactions on carbon, free protons, and electrons in the detector liquid. All four possible neutrinos,  $\nu_e$ ,  $\bar{\nu}_e$ ,  $\nu_\mu$ , and  $\bar{\nu}_\mu$ , contribute to neutral-current processes over the entire energy range. Charged-current cross sections are significantly affected by nuclear threshold effects. In the case of  $\nu_\mu$  and  $\bar{\nu}_\mu$  charged-current interactions, a large amount of the initial neutrino energy goes into the mass of the final state muon.

Neutrino processes that are observed in LSND are classified into three categories: standard model leptonic processes (e.g.  $\nu e \rightarrow \nu e$  elastic scattering), inverse  $\beta$ -decay processes, and semi-leptonic processes that leave excited or fragmented nuclei in the final state. Cross sections in the first category may be calculated to high accuracy, better than 1%, provided that the neutrino energy is known. Cross sections for the inverse  $\beta$ -decay reactions are inferred from the measured  $\beta$ -decay lifetimes and are accurate to the order of a few percent. (The momentum transfers are sufficiently small that form factor dependences are well characterized.) The cross sections for the reactions involving nuclear excited states are much less certain [15]. Models such as the continuum random phase approximation (CRPA) [16] often require large corrections in order to account for ground state wave functions that are too simplistic. Fermi Gas models do not reliably take into account nuclear effects but can be made to produce reasonable agreement in the quasi-elastic energy region when effective masses are employed [18, 19].

We use the results of a shell model calculation [15] for the  $^{12}\text{C}(\nu_e, e^-) ^{12}\text{N}$  DAR processes ( $E_\nu < 52.8$  MeV). The shell model calculation gives a similar energy shape but a lower cross section than the CRPA calculation [16]. A relativistic Fermi Gas model with an effective mass correction employed to account for nuclear effects is used for the more energetic DIF neutrino processes.

Two-body neutrino interactions are known accurately from either measurement or theory. Those processes are listed in Table IV with their associated cross section uncertainty. They provide the main constraints on neutrino fluxes, trigger and selection efficiencies, and other neutrino cross sections. Table IV also lists the neutrino flux sources constrained by each of these processes. For example, the  $^{12}\text{C}(\nu_e, e^-) ^{12}\text{N}_{g.s.}$  and the  $\nu e \rightarrow \nu e$  elastic reactions primarily constrain the rate of  $\mu^+$  DAR in the target area. Of all the  $^{12}\text{N}$  states, only

the ground state  $\beta$  decays, and the  $^{12}\text{C}(\nu_\mu, \mu^-) ^{12}\text{N}_{g.s.}$  reaction is the best measure of the  $\pi^+ \rightarrow \nu_\mu \mu^+$  DIF rate in the target area. Those reactions that contain a final state  $^{12}\text{N}_{g.s.}$  have nuclear matrix elements directly related to well known nuclear matrix elements, so that the cross sections may be calculated to an accuracy of a few percent. The  $\nu e \rightarrow \nu e$  elastic reactions are Standard Model electroweak calculations and are known to better than a percent from the measured weak mixing angle,  $\sin^2 \theta_W$ , and the Fermi constant,  $G_F$ .

Events in the LSND detector were simulated by using the GEANT3.21 code [17], which was modified to track optical photons in addition to ionizing particles. Neutrons were tracked and captured on free protons via the standard MICAP interface to GEANT. Optical photon yields from both scintillation and Čerenkov processes were generated and tracked to the photomultiplier tubes. A simulation of the photomultiplier response, analog and digital electronics, and event trigger produced event data packets, which were a good representation of the LSND detector response to neutrino events. A large sample of Michel decays from cosmic rays was used to check the quality of simulated events. The resulting neutrino event samples are then processed by the same reconstruction and particle identification software as the beam data. The reconstructed data are then compared to beam-excess data for the following analyses.

#### IV. DATA PROCESSING AND EVENT RECONSTRUCTION

A new event reconstruction that improved the position resolution and the spatial correlation between the  $e^+$  and neutron-capture  $\gamma$  in the reaction  $\bar{\nu}_e p \rightarrow e^+ n$  was applied to the entire 1993-1998 data sample. Different event samples were made during the new data reduction, and we focus here on the measurement of electron events, which are relevant to the oscillation search.

The electron selection was applied to the  $\sim 4$  Terabytes of raw LSND DLT data tapes, using a minimal set of cuts. This process achieved roughly a 40:1 reduction in data size, while maintaining an  $87 \pm 2\%$  efficiency for electron events, independent of electron energy above 20 MeV. Events in this new data stream that appeared in samples from previous LSND analyses were labelled, and a cross-check for consistency between new and old samples was performed.

Table V shows the electron reduction criteria and the corresponding efficiencies. First,

the visible energy was required to be greater than 15 MeV in order to eliminate  $^{12}\text{B}$   $\beta$  decays from cosmic ray  $\mu^-$  that stop and capture in the oil. Second, the number of associated veto hits was required to be less than 4. Third, events with a laser calibration tag were rejected. Fourth, loose electron particle identification criteria were imposed. Fifth, the resulting data were subjected to a loose fiducial volume cut, which required that the reconstructed electron vertex be inside a volume that was greater than 10 cm from the PMT surfaces. Finally, cosmic-ray muon events that produced decay electrons (Michel electrons) as the primary event were removed. In a clean sample of cosmic-ray Michel electron events there is a correlation between the total number of photoelectrons at the muon time and the online reconstructed distance to the subsequent Michel electron; as the cosmic muon becomes more energetic, the distance to the Michel electron grows linearly. A two dimensional region, or graphical cut, was imposed to remove these events.

The efficiency for electrons surviving the cuts was determined as follows. In an unbiased sample of laser-induced events with their associated accidental activities, a Monte Carlo (MC) electron event was inserted in place of the laser “primary”. This left a MC electron event in the midst of the accidental events from the real laser event. The MC electrons were generated flat in energy and uniformly throughout the tank. Desired accidental properties of the laser event, *e.g.* veto hit count and time to activities, were preserved when the electron MC event was inserted. Electron reduction criteria were then applied and the efficiencies calculated. The removal of accidental hits in time with the laser did not significantly affect the efficiency measurement.

Data were reprocessed with the new event reconstruction in order to improve the position resolution. The previous event reconstruction was limited due to the charge response of the 8” PMTs used in LSND (Hamamatsu R1408). For these PMTs, the single photoelectron output charge distribution is approximately a broad Gaussian plus an exponential tail that extends well above the mean of the Gaussian. As the position and angle fits weighted the hit PMTs by their charge, this charge tail has the effect of smearing the reconstructed event positions and angles. To ameliorate this effect, a new reconstruction algorithm was developed that weighted the hit PMTs by a ratio of the predicted charge to the square of the time resolution for that predicted charge,  $Q_{pred}/\sigma_t^2$ , and not by their measured charge,  $Q_{tube}$ . (The new reconstruction also has other improvements, such as the inclusion of timing information in the  $\gamma$  reconstruction.) This has resulted in an improvement in the position

correlation between the muon and the electron from stopped muon decay and between the neutron and the  $\gamma$  from neutron capture. The mean reconstructed distance between the muon and decay electron improved from 22 cm with the previous reconstruction to 14 cm with the current reconstruction. For 2.2 MeV  $\gamma$  from neutron capture, the most likely distance was reduced from 74 cm to 55 cm. As the accidental  $\gamma$  rate is proportional to the cube of this distance, the resulting  $\gamma$  reconstruction allows a cut on the  $R_\gamma$  parameter, as described later in section VII, that yields a factor of two better efficiency with a factor of two reduction in the rate of accidental  $\gamma$ s.

## V. PRIMARY ELECTRON SELECTION

The primary electron selection is next applied to the reduced data. The goal of the selection is to reduce the cosmic-ray background to as low a level as possible, while retaining a high efficiency for neutrino-induced electron events. The selection criteria and corresponding efficiencies are shown in Table V. The energy range  $20 < E < 200$  MeV is chosen so as to accept both DAR  $\bar{\nu}_\mu \rightarrow \bar{\nu}_e$  and DIF  $\nu_\mu \rightarrow \nu_e$  oscillation candidates. We require  $20 < E_e < 60$  MeV for the  $\bar{\nu}_\mu \rightarrow \bar{\nu}_e$  oscillation search and  $60 < E_e < 200$  MeV for the  $\nu_\mu \rightarrow \nu_e$  oscillation search. Below 20 MeV there are large backgrounds from the  $\beta$  decay of  $^{12}B$  created by the capture of stopped cosmic-ray  $\mu^-$  on  $^{12}C$ . Above 200 MeV the beam-related backgrounds from  $\pi^+ \rightarrow e^+\nu_e$  are large compared to any likely oscillation signal. Events with a previous activity within 12  $\mu s$ , a future activity within 8  $\mu s$ , or a bottom veto counter hit are rejected in order to eliminate cosmic-ray muon events. To further minimize cosmic-ray background, a tight electron particle identification is applied,  $-1.5 < \chi'_{tot} < 0.5$ , where the allowed range is chosen by maximizing the selection efficiency divided by the square root of the beam-off background with a correlated neutron. The  $\chi'_{tot}$  parameter depends on the product of the  $\chi$  parameters defined in [9]. Briefly,  $\chi_r$  and  $\chi_a$  are the quantities minimized for the determination of the event position and direction, and  $\chi_t$  is the fraction of PMT hits that occur more than 12 ns after the fitted event time. The dependence of the  $\chi$  parameters on energy and position for Michel electrons was studied, and a correction was developed that made  $\chi'_{tot}$  independent of energy or position. For the 1993 data only, which had an electronics timing problem resulting in a broader  $\chi'_{tot}$  distribution,  $0.3 < \chi_{tot}^{old} < 0.65$  was also required, where  $\chi_{tot}^{old}$  is computed like  $\chi'_{tot}$ , but with  $\chi$  parameters defined in reference

[1]. Additionally, the trigger time is required to occur between 85 ns and 210 ns in the 500 ns trigger window in order to reject multiple events, no veto hit is allowed within 30 ns of the trigger time, and the reconstructed electron vertex is required to be inside a volume 35 cm from the faces of the photomultiplier tubes. Finally, the number of associated  $\gamma$ s with  $R_\gamma > 10$  ( $R_\gamma$  is discussed in section VII) is required to be  $< 2$  ( $< 1$ ) for events  $< 60$  ( $> 60$ ) MeV in order to reject neutron-induced events, which tend to have many associated  $\gamma$ s. Neutrons from  $\bar{\nu}_e p \rightarrow e^+ n$  scattering are too low in energy ( $< 5$  MeV) to knock out other neutrons; however, higher energy neutrons ( $> 20$  MeV) typically knock out 1 or more neutrons. The event selection is identical for the DAR and DIF samples except for the associated  $\gamma$  criteria. Note that the event selection is optimized for electrons in the DAR energy range; however, it was applied to the DIF energy range for simplicity and in order that a common selection criteria be used over the entire interval from 20 – 200 MeV for oscillations from both DAR  $\bar{\nu}_\mu \rightarrow \bar{\nu}_e$  and DIF  $\nu_\mu \rightarrow \nu_e$ .

In addition to the electron reduction and selection efficiencies, Table V also shows the efficiencies due to the data acquisition (DAQ) and veto deadtime. The total efficiency for electrons in the fiducial volume with energies in the range  $20 < E_e < 60$  MeV is  $0.42 \pm 0.03$ .

## VI. CONVENTIONAL NEUTRINO PROCESSES

The neutrino oscillation analysis consists of two steps. The first step is to determine the best values for the numbers of events from standard neutrino processes in a way that minimizes the systematic uncertainty due to the electron selection. The second step is to use those measured neutrino backgrounds as central values in a fit to the oscillation parameters, allowing the backgrounds to vary around the central values within their uncertainty. The first step will be discussed in this section.

The inclusive electron data set provides a common selection for all neutrino processes important to the oscillation analysis. Some of these have well-determined cross sections: the  $^{12}\text{N}$  ground state events,  $\nu e$  elastic events, and  $\bar{\nu} p$  charged-current events. These events serve to constrain the neutrino fluxes and the selection efficiencies. They also provide important constraints on uncertain cross sections, such as  $^{12}\text{N}$  excited state events, where the nuclear response function is not well known.

Once the primary electron is selected, events are categorized by whether or not there are

associated events in the past or future of the primary. This categorization isolates most of the important reactions. The simplest event topology has an electron with no correlated event in the past or future, i.e. inclusive electrons. Ground state events are selected by searching for  $^{12}\text{N}$   $\beta$  decay within 70 ms and 70 cm of the primary electron event. Events from the process  $\bar{\nu}_e p \rightarrow e^+ n$  have a correlated  $\gamma$  from neutron capture within 1 ms. Muon neutrino induced events are selected efficiently because the Michel electron decay of the muon satisfies the primary electron criteria. The additional requirement of a prior event within 10  $\mu\text{s}$  efficiently finds the initial neutrino interaction muon event. The muon events can have, in addition, future events from neutron-capture  $\gamma$ s and nuclear  $\beta$  decays. A list of the various event categories is shown in Table VI.

A least squares fit was designed to find the best values for the neutrino fluxes, efficiencies, and cross sections. It fits those parameters by minimizing the  $\chi^2$  formed from the predicted number of events in various distributions compared to the observed number of events. The distributions are chosen to be sensitive to each of the parameters in question. Table VII lists the parameters adjusted in the fit, along with the fitted correction values, central correction values, and nominal parameter values. The central correction value is the Gaussian error by which each parameter was allowed to vary in the fit. The final fitted value for each parameter is the product of the nominal parameter value and the fitted correction value. The agreement between the data and the least squares fit is good. The fitted DIF neutrino flux and  $\pi^-/\pi^+$  ratio are about one sigma lower than the nominal values; however, the nominal values are used when estimating the neutrino background to the oscillation search. The  $\nu_\mu C \rightarrow \mu^- N^*$  cross section is lower than current theoretical predictions [15], [16] but is in agreement with our earlier measurement [21].

Fig. 5 shows the electron and  $\beta$  energy distributions and the time between the electron and  $\beta$ ,  $\Delta t$ , for  $^{12}\text{C}(\nu_e, e^-)^{12}\text{N}_{g.s.}$  scattering events. The energy and angular distributions for inclusive electron events are shown in Fig. 6, where  $E_e$  is the electron energy and  $\theta_\nu$  is the angle between the incident neutrino and outgoing electron directions. Neutrino-electron elastic scattering events are clearly visible near  $\cos\theta_\nu \sim 1$ . Fig. 7 shows the angular distribution in more detail (top plot) as well as the energy distribution (bottom plot) for the neutrino-electron elastic scattering events with  $\cos\theta_\nu > 0.9$  and with  $^{12}\text{C}(\nu_e, e^-)^{12}\text{N}_{g.s.}$  events removed. Fig. 8 shows the muon and  $\beta$  energy distributions and the time between the muon and  $\beta$  for  $^{12}\text{C}(\nu_\mu, \mu^-)^{12}\text{N}_{g.s.}$  scattering events. Finally, Fig. 9 shows the Michel

electron and muon energy distributions, the time between the muon and electron,  $\Delta t$ , and the distance between the reconstructed electron and muon positions,  $\Delta r$ , for  $\nu_\mu C \rightarrow \mu^- N$ ,  $\bar{\nu}_\mu C \rightarrow \mu^+ B$ , and  $\bar{\nu}_\mu p \rightarrow \mu^+ n$  inclusive scattering events. Cross sections for  $\nu C$  scattering based on a partial data sample have been published previously [20], [21]. Final cross sections for  $\nu e$  elastic scattering [22],  $\nu_e C$  scattering [23], and  $\nu_\mu C$  scattering [24] will be reported elsewhere and are consistent with the nominal parameter values shown in Table VII.

## VII. THE DECAY-AT-REST OSCILLATION ANALYSIS

### A. Signal and Background Reactions

The primary oscillation search in LSND is for  $\bar{\nu}_\mu \rightarrow \bar{\nu}_e$  oscillations, where the  $\bar{\nu}_\mu$  arise from  $\mu^+$  DAR in the beam stop and the  $\bar{\nu}_e$  are identified through the reaction  $\bar{\nu}_e p \rightarrow e^+ n$ . This reaction allows a two-fold signature of a positron with a 52 MeV endpoint and a correlated 2.2 MeV  $\gamma$  from neutron capture on a free proton. There are only two significant neutrino backgrounds with a positron/electron and a correlated neutron. The first background is from  $\mu^-$  DAR in the beam stop followed by  $\bar{\nu}_e p \rightarrow e^+ n$  scattering in the detector. As mentioned earlier, this background is highly suppressed due to the requirements that a  $\pi^-$  be produced, the  $\pi^-$  decays in flight, and the  $\mu^-$  decays at rest prior to capture. The  $\bar{\nu}_e$  flux is calculated to be only  $\sim 8 \times 10^{-4}$  relative to the  $\bar{\nu}_\mu$  flux in the  $20 < E_\nu < 52.8$  MeV energy range. The second background is from  $\pi^-$  DIF in the beam stop followed by  $\bar{\nu}_\mu p \rightarrow \mu^+ n$  scattering in the detector. (Additional contributions are from  $\bar{\nu}_\mu C \rightarrow \mu^+ n X$  and  $\nu_\mu C \rightarrow \mu^- n X$  scattering.) This background will mimic the oscillation reaction if the  $\mu^+$  is sufficiently low in energy that it is below the threshold of 18 hit PMTs, corresponding to  $E_\mu < 4$  MeV. Table VIII shows the estimated number of events in the  $20 < E_e < 60$  MeV energy range satisfying the electron selection criteria for 100%  $\bar{\nu}_\mu \rightarrow \bar{\nu}_e$  transmutation and for the two beam-related backgrounds with neutrons. Uncertainties in the efficiency, cross section, and  $\nu$  flux lead to systematic errors of between 10% and 50% for the signal and backgrounds discussed below.

The largest beam-related background with a correlated neutron is due to  $\bar{\nu}_e$  produced in the beam stop by conventional processes. Such events are identical to the oscillation candidates, and are identified via the reaction  $\bar{\nu}_e p \rightarrow e^+ n$ . Their most important source is the DAR of  $\mu^-$  in the beam stop. The total background due to intrinsic  $\bar{\nu}_e$  in the beam is

the product of neutrino flux ( $1.08 \times 10^{11} \bar{\nu}_e/cm^2$ ), average cross section over the entire energy range ( $0.72 \times 10^{-40} \text{ cm}^2$ ) [25], the number of free protons in the fiducial volume ( $7.4 \times 10^{30}$ ), the fraction of events with  $E > 20$  MeV (0.806), and the average positron reconstruction efficiency after cuts (0.42), which gives a total background of  $19.5 \pm 3.9$  events before any  $\gamma$  selection. Another possible source of  $\bar{\nu}_e$ , the direct decay of  $\pi^- \rightarrow e^- \bar{\nu}_e$ , is negligible, as a consequence of its low branching ratio ( $1.2 \times 10^{-4}$ ), the 1/8 ratio of  $\pi^-$  to  $\pi^+$  in the target, and the capture of  $\pi^-$  in the material of the beam dump.

A related background is due to  $\bar{\nu}_e \text{ }^{12}\text{C} \rightarrow e^+ \text{ }^{11}\text{B} n$  scattering. The cross section to the  $\text{ }^{12}\text{B}$  ground state is calculated to be  $6.3 \times 10^{-42} \text{ cm}^2$  [26], and the cross section to the  $\text{ }^{11}\text{B} n$  final state is estimated to be at least a factor of two smaller, especially because the first four excited states of  $\text{ }^{12}\text{B}$  are stable against neutron emission. Therefore, we estimate that this background is  $< 2\%$  of the  $\bar{\nu}_e p \rightarrow e^+ n$  background and is negligible. Furthermore, the maximum positron energy from this background is 36.1 MeV, so that almost all of the positrons are below 36 MeV.

The second most important source of beam-related background events with correlated neutrons is the misidentification of  $\bar{\nu}_\mu$  and  $\nu_\mu$  charged-current interactions as  $\bar{\nu}_e$  events. Because of the energy needed to produce a  $\mu$ , such a  $\bar{\nu}_\mu$  or  $\nu_\mu$  must arise from a  $\pi$  that decays in flight. In the tank the  $\bar{\nu}_\mu$  interacts by either  $\bar{\nu}_\mu p \rightarrow \mu^+ n$  or (less often)  $\bar{\nu}_\mu \text{C} \rightarrow \mu^+ n X$ , followed by  $\mu^+ \rightarrow e^+ \nu_e \bar{\nu}_\mu$ . The  $\nu_\mu$  interacts by  $\nu_\mu \text{C} \rightarrow \mu^- n X$ . There are four possible reasons for the misidentification. First, the muon can be missed because the  $\mu^+$  lifetime is  $> 12\mu\text{s}$  or the deposited energy is below the 18 phototube threshold for activity triggers. The latter can occur either because the muon is too low in energy or is produced behind the phototube surfaces. The detector Monte Carlo simulation is used to show that this threshold corresponds to a  $\mu$  kinetic energy,  $T_\mu$ , of approximately 3 MeV. The background rate from  $\bar{\nu}_\mu p \rightarrow \mu^+ n$  is written as the product of the total  $\bar{\nu}_\mu$  flux above threshold ( $2.56 \times 10^{11} \bar{\nu}_\mu/cm^2$ ), the average flux-weighted cross section ( $4.9 \times 10^{-40} \text{ cm}^2$ ) [25], the fraction of  $\mu^+$  having  $T_\mu < 3$  MeV or  $\tau_\mu > 12\mu\text{s}$  (0.0258), the number of free protons in the fiducial volume ( $7.4 \times 10^{30}$ ), the positron efficiency (0.42), and the fraction of events with  $E > 20$  MeV (0.816), for a background of 8.2 events. Similar estimates for the backgrounds from  $\bar{\nu}_\mu \text{C} \rightarrow \mu^+ n X$  and  $\nu_\mu \text{C} \rightarrow \mu^- n X$  [27] add 0.4 and 1.4 events, respectively, for a total of  $10.0 \pm 4.6$  events. It is estimated [27] that about 80% of the  $\bar{\nu}_\mu \text{C} \rightarrow \mu^+ X$  and 6% of the  $\nu_\mu \text{C} \rightarrow \mu^- X$  scattering events will have a recoil neutron.



Second, a  $\mu$  above the hit threshold can be missed if a prompt decay to  $e$  caused the muon and electron to be collected in a single event which is then misidentified as an  $e$ . This effect is considerably suppressed by the electron selection and the requirement that the reconstructed time be consistent with the triggered event time. The detector Monte Carlo simulation shows that this misidentification only occurs for  $\mu^+$  decays within 100 ns, decreases with  $T_\mu$ , and is almost zero above 10 MeV. Using the Monte Carlo misidentification probabilities, a calculation similar to that above implies a background of  $0.2 \pm 0.1$  events.

Third, the  $\mu^+$  can be lost because it is produced behind the PMT surface and the electron radiates a hard  $\gamma$  that reconstructs within the fiducial volume. A background of  $0.2 \pm 0.1$  events is estimated from the Monte Carlo simulation.

Fourth, a muon can be missed by trigger inefficiency. After 1994, we acquired for many online positron triggers complete digitization information for all veto and detector PMTs over the 6  $\mu\text{s}$  interval prior to the positron. Analysis of these data, discussed below, shows the trigger inefficiency for low-energy muons to be negligible.

There are additional backgrounds from  $\bar{\nu}_e$  produced by  $\mu^- \rightarrow e^- \nu_\mu \bar{\nu}_e$  and  $\pi^- \rightarrow e^- \bar{\nu}_e$  DIF. These  $\bar{\nu}_e$  can interact on either  $C$  or a free proton to yield the oscillation signature of a positron and a recoil neutron. For  $20 < E_e < 60$  MeV,  $0.1 \pm 0.1$  events are estimated. The reactions  $\nu_e \text{}^{12}\text{C} \rightarrow e^- n X$  and  $\nu_e \text{}^{13}\text{C} \rightarrow e^- n X$  are negligible ( $< 0.1$  events) over the  $20 < E_e < 60$  energy range and cannot occur for  $E_e > 20$  MeV and  $E_e > 36$  MeV, respectively. Other backgrounds, for example  $\nu_\mu C \rightarrow \nu_\mu n \gamma X$  with  $E_\gamma > 20$  MeV,  $\nu_e C \rightarrow e^- p X$  followed by  $\text{}^{13}\text{C}(p, n) \text{}^{13}\text{N}$ , and  $\nu_\mu C \rightarrow \mu^- X$  followed by  $\mu^-$  capture, are also negligible.

The total background due to pion and muon DIF is  $10.5 \pm 4.6$  events before any  $\gamma$  selection. It has a detected energy spectrum which is very close to that for positrons from  $\mu^+$  decay.

A final source of background is neutrons from the target that find their way into the detector tank. However, a stringent limit on beam neutron background relative to the cosmic neutron background has been set by looking for a beam-on minus beam-off excess of neutron events that pass neutron PID criteria in the 40-180 MeV electron equivalent range [2]. No excess has been observed, which implies that the beam-related neutron background is less than 1% of the total beam-unrelated background and is negligible.

The number of events expected for 100%  $\bar{\nu}_\mu \rightarrow \bar{\nu}_e$  transmutation followed by  $\bar{\nu}_e p \rightarrow e^+ n$  scattering (plus a small contribution from  $\bar{\nu}_e C \rightarrow e^+ B n$  scattering) is  $33300 \pm 3300$  events, where the systematic error arises from uncertainties in the neutrino flux (7%) and

$e^+$  efficiency (7%). This number of events is the product of neutrino flux ( $1.26 \times 10^{14} \nu/\text{cm}^2$ ), the average cross section [25] over the entire energy range ( $0.95 \times 10^{-40} \text{ cm}^2$ ), the average positron reconstruction efficiency (0.42), the fraction of events with  $E > 20 \text{ MeV}$  (0.894), and the number of free protons in the fiducial volume ( $7.4 \times 10^{30}$ ).

## B. The Positron Criteria

The positron/electron selection criteria (LSND is insensitive to the sign of the charge) for this primary oscillation search is described in detail in section V.

## C. The Correlated 2.2 MeV $\gamma$ Criteria

Correlated 2.2 MeV  $\gamma$  from neutron capture are distinguished from accidental  $\gamma$  from radioactivity by use of the likelihood ratio,  $R_\gamma$ , which is defined to be the likelihood that the  $\gamma$  is correlated divided by the likelihood that the  $\gamma$  is accidental.  $R_\gamma$  depends on three quantities: the number of hit PMTs associated with the  $\gamma$  (the multiplicity is proportional to the  $\gamma$  energy), the distance between the reconstructed  $\gamma$  position and positron position, and the time interval between the  $\gamma$  and positron (neutrons have a capture time in mineral oil of  $186 \mu\text{s}$ , while the accidental  $\gamma$  are uniform in time). Fig. 10 shows these distributions, which are obtained from fits to the data, for both correlated 2.2 MeV  $\gamma$  (solid curves) and accidental  $\gamma$  (dashed curves). To determine  $R_\gamma$ , the product of probabilities for the correlated distributions is formed and divided by the product of probabilities for the uncorrelated distributions. The accidental  $\gamma$  efficiencies are measured from the laser-induced calibration events, while the correlated  $\gamma$  efficiencies are determined from the Monte Carlo simulation of the experiment. Similar results for the correlated  $\gamma$  efficiencies are obtained from the cosmic-ray neutron events, whose high energy gives them a slightly broader position distribution. The efficiencies for different  $R_\gamma$  selections are shown in Table IX. The systematic uncertainty of these efficiencies is estimated to be  $\pm 7\%$  of their values. Note that with the new reconstruction, the correlated  $\gamma$  efficiency has increased while the accidental  $\gamma$  efficiency has decreased. For  $R_\gamma > 10$ , the correlated and accidental efficiencies are 0.39 and 0.003, respectively. For the previous reconstruction [2] the  $R_\gamma^{old} > 30$  cut gave correlated and accidental efficiencies of 0.23 and 0.006, respectively.

As checks of the likelihood distributions, Fig. 11 shows the  $R_\gamma$  distributions for  $\nu_e C \rightarrow e^- N_{g.s.}$  exclusive events [20], where the  $N_{g.s.}$   $\beta$  decays. By definition, the  $\nu_e C \rightarrow e^- N_{g.s.}$  reaction has no recoil neutron, so that its  $R_\gamma$  distribution should be consistent with a purely accidental  $\gamma$  distribution. A fit to the  $R_\gamma$  distribution finds that the fraction of events with a correlated  $\gamma$ ,  $f_c$ , is  $f_c = -0.004 \pm 0.007$  ( $\chi^2 = 4.6/9$  DOF). Fig. 12 shows the  $R_\gamma$  distribution for the sample of  $\mu^\pm$  events arising from the reactions  $\nu_\mu C \rightarrow \mu^- X$ ,  $\bar{\nu}_\mu C \rightarrow \mu^+ X$ , and  $\bar{\nu}_\mu p \rightarrow \mu^+ n$ . Correlated  $\gamma$  are expected for  $\sim 14\%$  of these events [27]. A fit to the  $R_\gamma$  distribution gives  $f_c = 0.129 \pm 0.013$  ( $\chi^2 = 8.2/9$  DOF), in agreement with expectations. Fig. 13 shows the distributions of  $\Delta r$ ,  $\Delta t$ , and  $N_{hits}$  for events with  $R_\gamma > 1$  (left side) and  $R_\gamma < 1$  (right side). The top plots show the distance between the reconstructed  $\gamma$  position and positron position,  $\Delta r$ , the middle plots show the time interval between the  $\gamma$  and positron,  $\Delta t$ , and the bottom plots show the number of hit PMTs associated with the  $\gamma$ ,  $N_{hits}$ .

#### D. Neutrino Oscillation Results

Table X shows the statistics for events that satisfy the selection criteria for the primary  $\bar{\nu}_\mu \rightarrow \bar{\nu}_e$  oscillation search. An excess of events is observed over that expected from beam-off and neutrino background that is consistent with neutrino oscillations. A  $\chi^2$  fit to the  $R_\gamma$  distribution, as shown in Fig. 14, gives  $f_c = 0.0567 \pm 0.0108$  ( $\chi^2 = 10.7/9$  DOF), which leads to a beam on-off excess of  $117.9 \pm 22.4$  events with a correlated neutron. Subtracting the neutrino background from  $\mu^-$  DAR followed by  $\bar{\nu}_e p \rightarrow e^+ n$  scattering ( $19.5 \pm 3.9$  events) and  $\pi^-$  DIF followed by  $\bar{\nu}_\mu p \rightarrow \mu^+ n$  scattering ( $10.5 \pm 4.6$  events) [28] leads to a total excess of  $87.9 \pm 22.4 \pm 6.0$  events, as shown in Table XI. This excess corresponds to an oscillation probability of  $(0.264 \pm 0.067 \pm 0.045)\%$ , where the first error is statistical and the second error is the systematic error arising from uncertainties in the backgrounds, neutrino flux (7%),  $e^+$  efficiency (7%), and  $\gamma$  efficiency (7%). Note that our previously published result [2], based on the 1993-1995 data sample, was  $(0.31 \pm 0.12 \pm 0.05)\%$ . Table XII shows the effect on the fitted oscillation probability of tightening some of the selection criteria.

A clean sample of oscillation candidate events can be obtained by requiring  $R_\gamma > 10$ , where as shown in Table X, the beam on-off excess is  $49.1 \pm 9.4$  events while the estimated neutrino background is only  $16.9 \pm 2.3$  events. Fig. 15 shows the individual  $\gamma$  distributions

for events with  $20 < E_e < 60$  MeV and with  $R_\gamma > 1$  (left side) and  $R_\gamma < 1$  (right side). The top plots show the distance between the reconstructed  $\gamma$  position and positron position,  $\Delta r$ , the middle plots show the time interval between the  $\gamma$  and positron,  $\Delta t$ , and the bottom plots show the number of hit PMTs associated with the  $\gamma$ ,  $N_{hits}$ . Fig. 16 displays the energy distribution of events with  $R_\gamma > 10$ . The shaded regions show the combination of neutrino background plus neutrino oscillations at low  $\Delta m^2$ . The data agree well with the oscillation hypothesis. As mentioned in section I, the 1993-1995 data runs employed a 30 cm water target, while the 1996-1998 data runs used a high-Z metal target. A comparison of the energy distributions of the two data samples is displayed in Fig. 17, which shows that the data samples are consistent within statistics.

Fig. 18 shows the  $\cos \theta_\nu$  distribution for events with  $R_\gamma > 1$  and  $36 < E_e < 60$  MeV. This energy range is chosen because it is particularly clean with reduced neutrino background, so that the  $\bar{\nu}_e p \rightarrow e^+ n$  reaction should dominate, while the  $\gamma$  requirement is relaxed to increase the statistics.  $\theta$  is the angle between the incident neutrino and outgoing positron directions. The shaded region in Fig. 18 shows the expected distribution from a combination of neutrino background plus neutrino oscillations. The  $\langle \cos \theta_\nu \rangle = 0.04 \pm 0.12$ , in agreement with the expectation of  $\sim 0.12$ .

Figs. 19 ( $D > 10$  cm) and 20 ( $D > 35$  cm) show the spatial distributions for events with  $R_\gamma > 10$  and  $20 < E_e < 60$  MeV, where  $z$  is along the axis of the tank (and approximately along the beam direction),  $y$  is vertical, and  $x$  is transverse. The shaded regions in Figs. 19 and 20 show the expected distributions from a combination of neutrino background plus neutrino oscillations. Fig. 21 shows scatter plots of the  $x$ - $y$  and  $y$ - $z$  spatial distributions for events with  $R_\gamma > 10$ ,  $20 < E_e < 60$  MeV, and  $D > 35$  cm. Figs. 22 and 23 show the  $\chi'_{tot}$  and veto hit distributions for events with  $R_\gamma > 10$  and  $20 < E_e < 60$  MeV. The solid histogram in the veto hit figure shows the distribution from  $\nu_e C \rightarrow e^- N_{g.s.}$  scattering. Finally, Fig. 24 shows the  $L_\nu/E_\nu$  distribution for events with  $R_\gamma > 10$  and  $20 < E_e < 60$  MeV, where  $L_\nu$  is the distance travelled by the neutrino in meters and  $E_\nu$  is the neutrino energy in MeV determined from the measured positron energy and angle with respect to the neutrino beam. The data agree well with the expectation from neutrino background plus neutrino oscillations at low  $\Delta m^2$  ( $\chi^2 = 4.9/8$  D.O.F.) or high  $\Delta m^2$  ( $\chi^2 = 5.8/8$  D.O.F.).

### E. Tests of the $\bar{\nu}_\mu \rightarrow \bar{\nu}_e$ Oscillation Hypothesis

A variety of tests of the  $\bar{\nu}_\mu \rightarrow \bar{\nu}_e$  oscillation hypothesis have been performed. One test of the oscillation hypothesis is to check whether there is an excess of events with more than one correlated  $\gamma$ . If the excess of events is indeed due to the reaction  $\bar{\nu}_e p \rightarrow e^+ n$ , then there should be no excess with more than one correlated  $\gamma$  because the recoil  $n$  is too low in energy ( $< 5$  MeV) to knock out additional neutrons. If, on the other hand, the excess involves higher energy neutrons ( $> 20$  MeV) from cosmic rays or the beam, then one would expect a large excess with  $> 1$  correlated  $\gamma$ , as observed in the beam-off cosmic ray data. However, as shown in Table XIII, the excess of events with more than one correlated  $\gamma$  is approximately zero for both the full  $20 < E_e < 60$  MeV energy region and the lower background  $36 < E_e < 60$  MeV energy region, as expected for the reaction  $\bar{\nu}_e p \rightarrow e^+ n$ .

Another test of the oscillation hypothesis is to check the “event lookback” for events that satisfy the oscillation criteria in order to ensure that the  $\bar{\nu}_\mu p \rightarrow \mu^+ n$  background is calculated correctly. The “event lookback” was installed prior to the 1995 running and consisted of an extra trigger that read out all hit detector PMTs in the  $6 \mu\text{s}$  interval before a primary event. Any background just below the 18 hit muon threshold will clearly show up, especially in the hit range with  $> 11$  lookback hits, where the probability of having an accidental lookback is only 5.6%. However, as shown in Table XIV, the excess of primary events with  $R_\gamma \geq 0$  or  $R_\gamma > 10$  is consistent with the accidental lookback probability. Thus, this “event lookback” check provides additional assurance that the  $\bar{\nu}_\mu p \rightarrow \mu^+ n$  background calculation of 10.5 events is not underestimated.

Both major backgrounds with a correlated neutron arise initially from  $\pi^-$  DIF. Therefore, a final test of the oscillation hypothesis is to check whether the  $\bar{\nu}_\mu$  flux from  $\pi^-$  DIF is correct. However, this has already been tested by the fit to the  $R_\gamma$  distribution, discussed above, of  $\nu_\mu C \rightarrow \mu^- X$ ,  $\bar{\nu}_\mu C \rightarrow \mu^+ X$ , and  $\bar{\nu}_\mu p \rightarrow \mu^+ n$  inclusive events [21]. For these reactions, correlated  $\gamma$  are expected for  $\sim 14\%$  of the events [27], due mainly to the  $\bar{\nu}_\mu$  flux. A fit to the  $R_\gamma$  distribution gives  $f_c = 0.129 \pm 0.013$  ( $\chi^2 = 8.2/9$  DOF), in agreement with expectation. Fig. 25 shows the time to the previous event for  $R_\gamma > 10$  electron events prior to applying the  $\Delta t_{past} > 12 \mu\text{s}$  selection. The top graph in the figure shows that the beam excess events are in agreement with our expectations for the  $\bar{\nu}_\mu p \rightarrow \mu^+ n$  and  $^{12}\text{C}(\bar{\nu}_\mu, \mu^+) ^{12}\text{B}^*$  channels. With the same data on a smaller vertical scale, the bottom graph shows events with accidental

past activities, in agreement with expectations from random cosmic ray backgrounds.

### VIII. THE DECAY-IN-FLIGHT OSCILLATION ANALYSIS

The high energy  $\nu_\mu$ s from  $\pi^+$  decay-in-flight are a potential source of  $\nu_\mu \rightarrow \nu_e$  oscillation events. The contamination of  $\nu_e$ s from standard sources is small, at the level of 0.1%. Unfortunately, the cosmic-ray backgrounds are large, with the result that the fluctuations in the beam-on, beam-off subtraction are comparable to the expected signal. Prior to 1996, it was realized that the 1996-1998 data would not support a stand alone, decay-in-flight analysis due to the larger beam-off backgrounds that are inherent in running with a heavy target. However, the analysis presented here is extended up to an electron energy of 200 MeV because the decay-in-flight data constrain the region  $> 2 \text{ eV}^2$ , especially around  $6\text{eV}^2$ .

The above analysis is applied to data in the energy range  $60 < E_e < 200 \text{ MeV}$ , with the additional requirement that there be no associated  $\gamma$ . This sample is only sensitive to  $\nu_\mu \rightarrow \nu_e$  oscillations, and results in a beam on-off excess of  $14.7 \pm 12.2$  events. The signal expected for 100%  $\nu_\mu$  to  $\nu_e$  transmutation is estimated to be 7800 events, and the  $\nu_e$  background from  $\mu^+ \rightarrow e^+ \bar{\nu}_\mu \nu_e$ ,  $\pi^+ \rightarrow e^+ \nu_e$ , and  $\nu e \rightarrow \nu e$  is estimated to be  $6.6 \pm 1.7$  events, resulting in a total excess of  $8.1 \pm 12.2 \pm 1.7$  events or an oscillation probability of  $(0.10 \pm 0.16 \pm 0.04)\%$ , as shown in Table XV. This result is lower than but consistent with our higher precision analysis of the 1993-1995 data sample [3]. That analysis determined the selection criteria by maximizing the acceptance divided by the square root of the beam-off background, which produced much less beam-off background overall. It gave a total excess of  $18.1 \pm 6.6 \pm 4.0$  oscillation events, corresponding to an oscillation probability of  $(0.26 \pm 0.10 \pm 0.05)\%$ . Due to changes in the neutrino production target, the 1996-1998 data sample had reduced DIF flux and higher beam-off background compared to the 1993-1995 data. Based on our DAR oscillation result and assuming that CP is conserved in the lepton sector, we would expect the DIF oscillation probability to be  $\sim 0.26\%$  at high  $\Delta m^2$  (where  $(1.27\Delta m^2 L_\nu/E_\nu) \gg 1$ ) and  $\sim 0.05\%$  at low  $\Delta m^2$  (where  $(1.27\Delta m^2 L_\nu/E_\nu) \ll 1$ ).

The 0.16% statistical error on the oscillation probability in the present analysis is larger than the 0.10% statistical error of the previous analysis. That is because the present analysis uses the electron selection criterion developed for the DAR region below 60 MeV, which is less effective in removing the background to electron events in the DIF region above 60

MeV. When compared to the previously published DIF analysis, the beam-off background for these higher energy events is 3.42 times higher in the present analysis, while the number of expected events for 100%  $\nu_\mu \rightarrow \nu_e$  transmutation is only 1.16 times higher. The previous analysis observed a 2.6 sigma excess, compared to the 0.6 sigma excess of the present analysis.

## IX. THE NEUTRINO OSCILLATION FIT

### A. Introduction

We describe in this section the  $(\sin^2 2\theta, \Delta m^2)$  likelihood ( $\mathcal{L}$ ) fitter. The fitter is applied to beam-on events in the final oscillation sample and calculates a likelihood in the  $(\sin^2 2\theta, \Delta m^2)$  plane in order to extract the favored oscillation parameters. The fit is similar to that performed in reference [29].

The  $\mathcal{L}$  product in the  $(\sin^2 2\theta, \Delta m^2)$  plane is formed over the individual beam-on events that pass the oscillation cuts. This three-dimensional contour is sliced to arrive finally at the LSND allowed oscillation region. The beam-related backgrounds are determined from MC event samples for each individual background contribution. The MC contains the trigger simulation and generally very well reproduces the tank response to all particles of interest. Agreement between the data and MC is excellent. The fit is over the entire electron energy range  $20 < E_e < 200$  MeV. Therefore, DIF oscillations and DIF backgrounds in addition to the usual DAR processes are considered.

### B. Formalism

Each beam-on event is characterized by four variables: the electron energy,  $E_e$ , the electron reconstructed distance along the tank axis,  $z$ , the reconstructed direction cosine the electron makes with the neutrino,  $\cos\theta_\nu$ , and the likelihood ratio that the event has a correlated 2.2 MeV  $\gamma$ ,  $R_\gamma$ . Each of the neutrino-induced background processes is simulated, and the simulation is compared to real events in the detector. Accidental  $\gamma$  events are used with real neutrino processes to simulate accidental events. Beam-off events are used as a background contribution after scaling by the measured time-dependent duty factor. The duty factor for this analysis was determined by using the entire raw event sample to measure

the ratio of beam-on time to beam-off time. The raw event sample consists mostly of beta-decay events and is, to a good approximation, unbiased by beam-related events. The duty factor for each run was determined by dividing the number of raw events when the beam-on bit was set by the number of raw events where it was not set. This resulted in a duty factor for each run that was used to weight the beam-off events to determine the beam-unrelated subtraction for the final event sample.

For every point in the  $(\sin^2 2\theta, \Delta m^2)$  plane, oscillation signal events are generated to complete the description of sources expected in the beam-on sample. There are 5697 beam-on events in the data sample, and a likelihood is calculated for each one based on the values of  $E_e$ ,  $z$ ,  $\cos \theta_\nu$  and  $R_\gamma$ .

Formally, each neutrino beam-on event  $j$  is assigned a probability  $p_j(E_e, z, \cos \theta_\nu, R_\gamma)$  equal to a sum of probabilities  $q_i(E_e, z, \cos \theta_\nu, R_\gamma)$  from the backgrounds plus oscillations. It then remains to add the  $q_i$  with expected fractional contributions  $r_i$  and take the product over all the beam-on events. The likelihood is thus

$$\mathcal{L} = \left( \prod_{j=1}^{N_{\text{beam-on}}} p_j \right), \quad (9.1)$$

where

$$p_j(E_{ej}, R_{\gamma j}, \cos \theta_{\nu j}, z_j) = \sum_{i=1}^{N_{\text{contributions}}} q_i(E_{ej}, R_{\gamma j}, \cos \theta_{\nu j}, z_j) \cdot r_i. \quad (9.2)$$

Additionally, two normalization requirements must hold:

$$\sum_{i=1}^{N_{\text{contributions}}} r_i = 1, \quad (9.3)$$

and

$$\int dE_e dR_\gamma d(\cos \theta_\nu) dz q_i(E_e, R_\gamma, \cos \theta_\nu, z) = 1 \quad (9.4)$$

for each contribution,  $i$ . Together, these requirements ensure that every observed beam-on event has a probability of occurrence equal to 1.

### C. Background Variation

It is necessary to allow for the fact that the backgrounds are not perfectly known. The background variation is performed by calculating the above likelihood at each point in the  $(\sin^2 2\theta, \Delta m^2)$  plane many times, varying over the expected  $\sigma$  for each background. For each



background configuration, the  $\mathcal{L}$  is weighted with a Gaussian factor for each background that is off its central value. The background configurations are varied so that the beam-unrelated background (BUB) varies independently and the beam-related backgrounds (BRBs) are locked together. Different background varying procedures give very similar results.

#### D. The expression for the Likelihood

Finally, the likelihood can be expressed as

$$\mathcal{L} = \int \mathcal{D}N_{bgd} \exp(-(N_{bgd} - N_{bgd,exp})^2/2\sigma^2) \cdot \left( \prod_{i=1}^{N_{beam-on}} p_i \right), \quad (9.5)$$

where the  $\int \mathcal{D}N_{bgd}$  represents, schematically, the background variation described above.

#### E. The Input

The  $q_i$  for each of the background and signal processes are all generated from the MC, except for the BUB  $q_i$ , which is generated from the beam-off data events. There are separate MC runs for each of the above BRB processes. Some of these backgrounds are grouped together (appropriately weighted) into a few common  $q_i$ s for easier bookkeeping, as indicated in Table XVI. This is done for backgrounds which don't need to be separately varied. Several small, beam-related backgrounds, DIF  $\nu e \rightarrow \nu e$  elastic scattering and  $\pi^+ \rightarrow e^+ \nu_e$  DAR followed by  $\nu_e C \rightarrow e^- N$  scattering, are contained in their DAR and DIF counterparts.

#### F. Slicing the contour

##### 1. The Feldman-Cousins Method

The Feldman-Cousins method [30] can be applied to the LSND  $\mathcal{L}$  contour in the following way. At a particular point in the  $(\sin^2 2\theta, \Delta m^2)$  plane, create thousands of generated data sets comprised of background and oscillations. For each Monte Carlo experiment compute  $\delta L = L_{Max} - L_{MC}$ , where  $L = \log \mathcal{L}$ ,  $L_{MC}$  is  $L$  at the particular point in the  $(\sin^2 2\theta, \Delta m^2)$  plane assumed in the Monte Carlo, and  $L_{Max}$  is the log likelihood at the values of  $\sin^2 2\theta$  and  $\Delta m^2$  that maximize  $\mathcal{L}$ . From a histogram of  $\delta L$  for the thousands of Monte Carlo data sets one obtains the selection that contains, for example, 90% of the experiments. Finally,

determine this selection at many points in the  $(\sin^2 2\theta, \Delta m^2)$  plane. The resulting function of  $\sin^2 2\theta$  and  $\Delta m^2$  corresponds to the 90% C.L. allowed LSND region.

This approach, as practiced in reference [29], required large amounts of CPU. Even scanning a judiciously chosen  $(\sin^2 2\theta, \Delta m^2)$  region is CPU intensive, and setting up and running the generated data sets would take many months. Therefore, the full Feldman-Cousins method will not be followed here. As shown below, using slices derived from a different LSND data set to determine the  $\mathcal{L}$  contours for this data set, the results obtained with the Feldman-Cousins method are similar to other methods.

### 2. *The Bayes Method*

For the Bayes method one presumes a prior expectation of the oscillation parameters from 0.01 to 100.0 eV<sup>2</sup> in  $\Delta m^2$  and 0.001 to 1.0 in  $\sin^2 2\theta$ . The assumption of this prior expectation is what makes this approach Bayesian. Each bin in the  $(\sin^2 2\theta, \Delta m^2)$  plane is assigned a weight  $w$ , where  $w = \delta x \delta y \cdot \mathcal{L}$ . That is, the weight is the measure of the probability distribution times the  $\mathcal{L}$ . The measure  $\delta x \delta y$  is taken to be  $\delta(\ln \sin^2 2\theta) \delta(\ln \Delta m^2)$ . The 90% and 99% C.L. regions are then determined by integrating over the  $(\sin^2 2\theta, \Delta m^2)$  plane.

### 3. *The Constant-Slice Method*

The constant-slice method makes a slice at a constant value of  $L$ . If, for example, the log likelihood were a two-dimensional Gaussian, slices of 2.3 and 4.6 units down from the peak  $L$  would correspond to 90% and 99% C.L., respectively. Fig. 26 shows that the Feldman-Cousins, Bayesian, and constant-slice methods all give about the same 90% regions. Note that for the Feldman-Cousins method the slices are derived from a different LSND data set. We use the constant-slice method in this paper to denote the favored regions in the  $(\sin^2 2\theta, \Delta m^2)$  plane.

## G. **Statistical Issues and Technical Hurdles**

Preserving correlations in the  $E_e, R_\gamma, \cos \theta_\nu, z$  parameter space over which the  $\mathcal{L}$  fit is performed is sometimes difficult, due to the fact that for certain backgrounds the 3600 bin

parameter space is too large to characterize. In particular,  $R_\gamma$ , with its logarithmic behavior for backgrounds in which uncorrelated  $\gamma$ s are present, is especially difficult. This problem was resolved for the BUB by binning the other parameters very coarsely, effectively ignoring correlations in some regions of the four-dimensional parameter space. Statistical problems with the MC BRB sample, in which uncorrelated  $\gamma$ s are present, were dealt with in a similar manner. Such measures were safe approximations for the fiducial volume of interest.

Other technical difficulties in certain ranges of  $\Delta m^2$  were overcome with weighting techniques. The origin of the difficulties was always one of limited statistical samples that characterized the probability distribution functions for the backgrounds. Another problem involved re-weighting by  $\sin^2(1.27\Delta m^2 \frac{L_\nu}{E_\nu})$ , which required prohibitive numbers of MC events and the simultaneous breaking of correlations in the four-dimensional space. However, these difficulties were overcome by smearing  $L_\nu$ , the distance travelled by the neutrino, and  $E_\nu$ , the neutrino energy, with the Gaussian widths determined from the position and energy resolutions.

## H. Results

A  $(\sin^2 2\theta, \Delta m^2)$  oscillation parameter fit for the entire data sample,  $20 < E_e < 200$  MeV, is shown in Fig. 27. The fit includes both  $\bar{\nu}_\mu \rightarrow \bar{\nu}_e$  and  $\nu_\mu \rightarrow \nu_e$  oscillations, as well as all known neutrino backgrounds. The inner and outer regions correspond to 90% and 99% CL allowed regions, while the curves are 90% CL limits from the Bugey reactor experiment [31], the CCFR experiment at Fermilab [32], the NOMAD experiment at CERN [33], and the KARMEN experiment at ISIS [34]. The most favored allowed region is the band from  $0.2 - 2.0 \text{ eV}^2$ , although a region around  $7 \text{ eV}^2$  is also possible, but has been made less probable by the  $\nu_\mu \rightarrow \nu_e$  analysis.

The KARMEN experiment also searches for  $\bar{\nu}_\mu \rightarrow \bar{\nu}_e$  oscillations with a detector that is similar to LSND. A comparison of the two experiments is given in Table XVII. LSND is a more massive detector, has a higher intensity neutrino source, and has good particle identification, while KARMEN has better energy resolution and the advantage of a much lower duty factor that helps eliminate cosmic-ray events. In addition, KARMEN is located 17.5 m from the neutrino source, compared with 30 m for LSND. Therefore, the experiments have sensitivities that peak at different values of  $\Delta m^2$ . At low  $\Delta m^2$ , for example, an

experiment at 30 m is 2.94 times more sensitive to neutrino oscillations than an experiment at 17.5 m. Note that a global analysis of the two experiments was performed by Eitel [29] using intermediate data sets.

The event breakdown from the  $20 < E < 200$  MeV four-dimensional fit is shown in Table XVI at the best-fit point

$$(\sin^2 2\theta, \Delta m^2)_{best-fit} = (0.003, 1.2\text{eV}^2).$$

The number of  $\bar{\nu}_\mu \rightarrow \bar{\nu}_e$  oscillation events at the best-fit point is 89.5 events, which agrees well with the  $87.9 \pm 22.4 \pm 6.0$  event excess from the fit to the  $R_\gamma$  distribution. The whole low  $\Delta m^2$  region gives an almost equally good fit within 0.5 log-likelihood units. Projections onto  $E_e, R_\gamma, z, \cos \theta_\nu$  from the four-dimensional fit at the best fit value of  $(\sin^2 2\theta, \Delta m^2)$  are plotted in Fig. 28. The fit is relatively insensitive to the starting values and gives good overall agreement with the data.

## X. CONCLUSIONS

The final LSND  $\bar{\nu}_\mu \rightarrow \bar{\nu}_e$  oscillation results are presented for all six years of data collection, 1993-1998. The analysis employed a new event reconstruction that greatly improved the correlation of the  $e^+$  and 2.2 MeV  $\gamma$  from the reaction  $\bar{\nu}_e p \rightarrow e^+ n$ , thus greatly reducing the background from neutrino events followed by an accidental  $\gamma$ . These final results are consistent with our earlier analysis of the 1993-1995 data sample [2]; in particular, the results from the 1993-1995 data sample, which used a water target, are consistent with the results from 1996-1998, which made use of a high- $Z$  target.

A global fit was performed to all event categories shown in Table VI in order to check our understanding of neutrino processes in the experiment. The parameters resulting from this fit, shown in Table VII, together with neutrino oscillations, yield a good description of all the observed data.

The LSND experiment provides evidence for neutrino oscillations from the primary  $\bar{\nu}_\mu \rightarrow \bar{\nu}_e$  oscillation search. A total excess of  $87.9 \pm 22.4 \pm 6.0$   $\bar{\nu}_e p \rightarrow e^+ n$  events with  $e^+$  energy between 20 and 60 MeV is observed above expected neutrino-induced backgrounds. This excess corresponds to an oscillation probability of  $(0.264 \pm 0.067 \pm 0.045)\%$ . A fit to all of the LSND neutrino processes determines the allowed oscillation parameters in a two-

generation model. In conjunction with other available neutrino oscillation limits, the LSND data suggest that neutrino flavor oscillations occur with a  $\Delta m^2$  in the range  $0.2 - 10 \text{ eV}^2/c^4$ .

In addition, using the same event selection, results are also presented for the decay-in-flight energy region. Although a clear event excess is not observed, the results are consistent with the  $\bar{\nu}_\mu \rightarrow \bar{\nu}_e$  oscillation signal and with our higher precision analysis of the 1993-1995 data sample [3], which determined the selection parameters by maximizing the acceptance divided by the square root of the beam-off background and which had much less beam-off background overall.

At present, the LSND results remains the only evidence for appearance neutrino oscillations and implies that at least one neutrino has a mass greater than  $0.4 \text{ eV}/c^2$ . The MiniBooNE experiment at Fermilab [35], which is presently under construction, is expected to provide a definitive test of the LSND results, and if the neutrino oscillation results are confirmed, will make a precision measurement of the oscillation parameters.

*Acknowledgments* This work was conducted under the auspices of the US Department of Energy, supported in part by funds provided by the University of California for the conduct of discretionary research by Los Alamos National Laboratory. This work is also supported by the National Science Foundation. We are particularly grateful for the extra effort that was made by these organizations to provide funds for running the accelerator at the end of the data taking period in 1995. It is pleasing that a large number of undergraduate students from participating institutions were able to contribute significantly to the experiment. We thank K. Eitel for his valuable contributions to the analysis.

TABLE I: The proton beam statistics for each of the years of running, 1993 through 1998.

Year	Charge (C)	Protons ( $\times 10^{22}$ )	A6 target	Active Targets
1993	1787	1.12	water	A1, A2, A6
1994	5904	3.69	water	A1, A2, A6
1995	7081	4.42	water	A1, A2, A6
1996	3789	2.37	high-Z metal	A6 & partial A2
1997	7181	4.48	high-Z metal	A6 only
1998	3154	1.97	high-Z metal	A6 only

TABLE II: The  $\mu^-$  absorption rates for materials in the target area [12].

Material	Z	$\mu^-$ Absorption Rate ( $\mu s^{-1}$ )
H	1	$0.00042 \pm 0.00002$
Be	4	$0.0074 \pm 0.0005$
C	6	$0.0388 \pm 0.0005$
O	8	$0.1026 \pm 0.0006$
Al	13	$0.7054 \pm 0.0013$
Fe	26	$4.411 \pm 0.024$
Cu	29	$5.676 \pm 0.037$
Zn	30	$5.834 \pm 0.039$
Mo	42	$9.61 \pm 0.15$
Ta	73	$12.86 \pm 0.13$
Pb	82	$13.45 \pm 0.18$
U	92	$12.60 \pm 0.04$

TABLE III: Average neutrino fluxes in LSND. Both decay at rest (DAR) and decay in flight (DIF) are shown in  $\nu/\text{cm}^2$ . The  $\nu_\mu$  and  $\bar{\nu}_\mu$  DIF fluxes are above  $\mu$  production threshold.

Source	Type	1993-1995 Flux	1996-1998 Flux	Total Flux
$\mu^+$ DAR	$\bar{\nu}_\mu$ and $\nu_e$	$7.38 \times 10^{13}$	$5.18 \times 10^{13}$	$1.26 \times 10^{14}$
$\mu^-$ DAR	$\nu_\mu$ and $\bar{\nu}_e$	$5.96 \times 10^{10}$	$4.87 \times 10^{10}$	$1.08 \times 10^{11}$
$\pi^+$ DIF	$\nu_\mu$	$1.37 \times 10^{12}$	$8.26 \times 10^{11}$	$2.20 \times 10^{12}$
$\pi^-$ DIF	$\bar{\nu}_\mu$	$1.45 \times 10^{11}$	$1.11 \times 10^{11}$	$2.56 \times 10^{11}$
$\pi^+$ DIF	$\nu_e$	$5.56 \times 10^8$	$5.01 \times 10^8$	$1.06 \times 10^9$
$\mu^+$ DIF	$\nu_e$	$4.13 \times 10^9$	$2.44 \times 10^9$	$6.57 \times 10^9$

TABLE IV: Cross section uncertainties for the neutrino reactions with two-body final states that occur in LSND. The cross sections for these processes are known accurately because either related measurements can be used to constrain the matrix elements or only fundamental particles are observed. Also shown are the corresponding neutrino flux constraints.

Process	$\sigma$ Constraint	$\sigma$ Uncertainty	Flux Constraint
$\nu e \rightarrow \nu e$	Standard Model Process	1%	$\mu^+ \rightarrow \nu_e \bar{\nu}_\mu e^+$ DAR
$^{12}\text{C}(\nu_e, e^-)^{12}\text{N}_{g.s.}$	$^{12}\text{N}_{g.s.}$	5%	$\mu^+ \rightarrow \nu_e \bar{\nu}_\mu e^+$ DAR
$^{12}\text{C}(\nu_\mu, \mu^-)^{12}\text{N}_{g.s.}$	$^{12}\text{N}_{g.s.}$	5%	$\pi^+ \rightarrow \nu_\mu \mu^+$ DIF
$p(\bar{\nu}_\mu, \mu^+)n$	neutron decay	5%	$\pi^- \rightarrow \bar{\nu}_\mu \mu^-$ DIF

TABLE V: The average efficiencies for electrons in the fiducial volume with energies in the range  $20 < E_e < 60$  MeV.

Criteria	Efficiency
Electron Reduction	
Energy > 15 MeV	1.00
Veto Hits < 4	$0.98 \pm 0.01$
No Laser Tag	1.00
Loose Electron PID	$0.96 \pm 0.01$
Vertex > 10 cm from PMTs	1.00
Cosmic Muon Cut	$0.92 \pm 0.01$
Electron Selection	
$\Delta t_{past} > 12\mu s$	$0.96 \pm 0.01$
$\Delta t_{future} > 8\mu s$	$0.99 \pm 0.01$
No bottom veto hit	1.00
$-1.5 < \chi'_{tot} < 0.5$	$0.84 \pm 0.01$
$0.3 < \chi_{tot}^{old} < 0.65$ (1993 only)	$0.98 \pm 0.01$
$85\text{ns} < t_{\text{event}} < 210\text{ns}$	1.00
$\Delta t_{veto}^{best} > 30\text{ns}$	$0.97 \pm 0.01$
$D > 35$ cm	$0.88 \pm 0.02$
$N_\gamma < 1, E > 60$	1.00
$N_\gamma < 2, E < 60$	1.00
Deadtime	
DAQ & Tape Deadtime	$0.96 \pm 0.02$
Veto Deadtime	$0.76 \pm 0.02$
Total	$0.42 \pm 0.03$



TABLE VI: Event categories used to determine the number of events from standard neutrino processes.

Category	Past Event	Primary Event	Future Event
$e$	-	$\nu_e$	-
$e \beta$	-	$\nu_e$	$^{12}N$ decay
$e \gamma$	-	$\nu_e$	$n$ capture
$\mu e$	$\mu$	$e(\text{muon decay})$	-
$\mu e \beta$	$\mu$	$e(\text{muon decay})$	$^{12}N$ decay
$e \gamma \beta$	-	$\nu_e$	accidental $\gamma + ^{12}N$ decay
$\mu e \gamma$	$\mu$	$e(\text{muon decay})$	$n$ capture
$e \text{ no } \beta$	-	$\nu_e$	-

TABLE VII: Parameters adjusted during the least squares fit procedure, along with the fitted correction values, central correction values, and nominal parameter values.

Parameter	Fitted Correction Value	Central Correction Value	Nominal Parameter Value
Flux Parameters			
$\Phi_{DIF}$	$0.88 \pm 0.09$	$1.00 \pm 0.15$	$0.22 \times 10^{13} \nu/cm^2$
$\Phi_{DAR}$	$1.01 \pm 0.05$	$1.00 \pm 0.07$	$12.6 \times 10^{13} \nu/cm^2$
$\frac{\pi^-}{\pi^+}$ ratio	$0.90 \pm 0.19$	$1.00 \pm 0.10$	0.12
Cross Section Parameters			
$\sigma(\nu_\mu^{12}C \rightarrow \mu^- {}^{12}N^*)$	$0.68 \pm 0.23$	$1.00 \pm 0.25$	$15.2 \times 10^{-40} cm^2$
$\sigma(\bar{\nu}_\mu p \rightarrow \mu^+ n)$	$0.97 \pm 0.05$	$1.00 \pm 0.05$	$4.9 \times 10^{-40} cm^2$
$\sigma(\nu_e^{12}C \rightarrow e^- {}^{12}N_{g.s.})$	$1.01 \pm 0.05$	$1.00 \pm 0.05$	$9.2 \times 10^{-42} cm^2$
$\sigma(\nu_e^{12}C \rightarrow e^- {}^{12}N^*)$	$1.02 \pm 0.13$	$1.00 \pm 0.25$	$4.1 \times 10^{-42} cm^2$
$\sigma(\nu_e^{13}C \rightarrow e^- {}^{13}N)$	$0.93 \pm 0.28$	$1.00 \pm 0.30$	$0.53 \times 10^{-40} cm^2$
Efficiency Parameters			
$\epsilon_\mu$	$1.00 \pm 0.06$	$1.00 \pm 0.07$	0.93
$\epsilon_\beta$	$1.00 \pm 0.04$	$1.00 \pm 0.07$	0.65
$\epsilon_e$	$1.00 \pm 0.05$	$1.00 \pm 0.07$	0.42
$\epsilon_\gamma$	$0.91 \pm 0.03$	$1.00 \pm 0.07$	0.60
duty ratio	$0.95 \pm 0.03$	$1.00 \pm 0.03$	0.060

TABLE VIII: The estimated number of events in the  $20 < E_e < 60$  MeV energy range due to 100%  $\bar{\nu}_\mu \rightarrow \bar{\nu}_e$  transmutation and to the two beam-related backgrounds with neutrons,  $\mu^-$  decay at rest in the beam stop followed by  $\bar{\nu}_e p \rightarrow e^+ n$  scattering in the detector and  $\pi^-$  decay in flight in the beam stop followed by  $\bar{\nu}_\mu p \rightarrow \mu^+ n$  scattering. The  $\pi^-$  DIF background includes contributions from  $\bar{\nu}_\mu C \rightarrow \mu^+ n X$  and  $\nu_\mu C \rightarrow \mu^- n X$  scattering, as well as a small  $\bar{\nu}_e$  background from  $\pi^-$  and  $\mu^-$  DIF. The events must satisfy the electron selection criteria, but no correlated  $\gamma$  requirement is imposed.

Neutrino Source	Reaction	Number of Events
$\mu^+$ DAR	100% $\bar{\nu}_\mu \rightarrow \bar{\nu}_e$	$33300 \pm 3300$
$\mu^-$ DAR	$\bar{\nu}_e p \rightarrow e^+ n$	$19.5 \pm 3.9$
$\pi^-$ DIF	$\bar{\nu}_\mu p \rightarrow \mu^+ n$	$10.5 \pm 4.6$

TABLE IX: The correlated and accidental  $\gamma$  efficiencies for different  $R_\gamma$  selections. The systematic uncertainty of these efficiencies is estimated to be  $\pm 7\%$  of their values.

Selection	Correlated $\gamma$ Efficiency	Accidental $\gamma$ Efficiency
$R_\gamma > 1$	0.51	0.012
$R_\gamma > 10$	0.39	0.0026
$R_\gamma > 100$	0.17	0.0002

TABLE X: Numbers of beam-on events that satisfy the selection criteria for the primary  $\bar{\nu}_\mu \rightarrow \bar{\nu}_e$  oscillation search with  $R_\gamma > 1$ ,  $R_\gamma > 10$ , and  $R_\gamma > 100$ . Also shown are the beam-off background, the estimated neutrino background, the excess of events that is consistent with neutrino oscillations, and the probability that the excess is due to a statistical fluctuation.

Selection	Beam-On Events	Beam-Off Background	$\nu$ Background	Event Excess	Probability
$R_\gamma > 1$	205	$106.8 \pm 2.5$	$39.2 \pm 3.1$	$59.0 \pm 14.5 \pm 3.1$	$7.8 \times 10^{-6}$
$R_\gamma > 10$	86	$36.9 \pm 1.5$	$16.9 \pm 2.3$	$32.2 \pm 9.4 \pm 2.3$	$1.1 \times 10^{-4}$
$R_\gamma > 100$	27	$8.3 \pm 0.7$	$5.4 \pm 1.0$	$13.3 \pm 5.2 \pm 1.0$	$1.8 \times 10^{-3}$

TABLE XI: The number of excess events in the  $20 < E_e < 60$  MeV energy range, together with the corresponding oscillation probability if the excess is due to  $\bar{\nu}_\mu \rightarrow \bar{\nu}_e$  oscillations. Also shown are the results from the analysis of the 1993-1995 data sample [2].

Analysis	Excess Events	Oscillation Probability
Present Analysis (1993-1998)	$87.9 \pm 22.4 \pm 6.0$	$(0.264 \pm 0.067 \pm 0.045)\%$
Previous Analysis (1993-1995)	$51.0^{+20.2}_{-19.5} \pm 8.0$	$(0.31 \pm 0.12 \pm 0.05)\%$

TABLE XII: The oscillation probabilities obtained with various selections. The  $S > 0.5$  selection was used in the previous analysis [2]. The nominal values are shown in Table XI

Selection	Oscillation Probability
Nominal	$(0.264 \pm 0.067 \pm 0.045)\%$
Nominal + $\Delta t_{past} > 20\mu s$	$(0.220 \pm 0.064 \pm 0.045)\%$
Nominal + Veto Hits $< 2$	$(0.303 \pm 0.074 \pm 0.045)\%$
Nominal + $-1.5 < \chi'_{tot} < 0$	$(0.304 \pm 0.077 \pm 0.045)\%$
Nominal + $D > 50$ cm & $Y > -50$ cm	$(0.252 \pm 0.071 \pm 0.045)\%$
Nominal + $D > 75$ cm	$(0.222 \pm 0.074 \pm 0.045)\%$
Nominal + $Y > -120$ cm	$(0.239 \pm 0.061 \pm 0.045)\%$
Nominal + $\Delta t_{past} > 15.2\mu s$ & $Y > -120$ cm	$(0.193 \pm 0.055 \pm 0.045)\%$
Nominal + $S > 0.5$	$(0.293 \pm 0.069 \pm 0.045)\%$

TABLE XIII: Number of beam on-off excess events that satisfy the selection criteria for the primary  $\bar{\nu}_\mu \rightarrow \bar{\nu}_e$  oscillation search with 1 associated  $\gamma$  and with  $> 1$  associated  $\gamma$ . (An associated  $\gamma$  is defined to have  $R_\gamma > 10$ .) The excess of events with  $> 1$  correlated  $\gamma$  is approximately zero, which is what is expected for the reaction  $\bar{\nu}_e p \rightarrow e^+ n$ .

Energy Selection	1 Associated $\gamma$	$> 1$ Associated $\gamma$
$20 < E_e < 60$ MeV	$49.1 \pm 9.4$	$-2.8 \pm 2.4$
$36 < E_e < 60$ MeV	$28.3 \pm 6.6$	$-3.0 \pm 1.7$

TABLE XIV: Number of beam on-off excess events that satisfy the selection criteria for the primary  $\bar{\nu}_\mu \rightarrow \bar{\nu}_e$  oscillation search with  $36 < E_e < 60$  MeV and with  $> 11$  “lookback” hits in the 0-3  $\mu\text{s}$  and 3-6  $\mu\text{s}$  intervals. Results are shown for events with  $R_\gamma \geq 0$  and for events with  $R_\gamma > 10$ . The number of excess events in each 3 $\mu\text{s}$  interval is consistent with the probability of having an accidental lookback in the time interval.

$R_\gamma$ Selection	0 – 3 $\mu\text{s}$	3 – 6 $\mu\text{s}$	Events Expected Due to Accidentals
$R_\gamma \geq 0$	$11.5 \pm 6.3$	$7.8 \pm 5.9$	$10.8 \pm 2.2$
$R_\gamma > 10$	$1.7 \pm 1.4$	$0.5 \pm 1.0$	$1.6 \pm 0.4$

TABLE XV: The number of excess events in the  $60 < E_e < 200$  MeV energy range, together with the corresponding oscillation probability if the excess is due to  $\nu_\mu \rightarrow \nu_e$  oscillations. Also shown are the results from the higher precision analysis of the 1993-1995 data sample [3].

Analysis	Excess Events	Oscillation Probability
Present Analysis (1993-1998)	$8.1 \pm 12.2 \pm 1.7$	$(0.10 \pm 0.16 \pm 0.04)\%$
Previous Analysis (1993-1995)	$18.1 \pm 6.6 \pm 4.0$	$(0.26 \pm 0.10 \pm 0.05)\%$

TABLE XVI: The eight contributions to the  $(\sin^2 2\theta, \Delta m^2)$   $\mathcal{L}$  fit from all of the signal and background processes. Also shown are the fitted number of events at the best fit point of  $(\sin^2 2\theta, \Delta m^2)_{best-fit} = (0.003, 1.2\text{eV}^2)$ .

$\mathcal{L}$ Contribution	Signal or Background Source	Process	Fitted Number of Events
1	$\bar{\nu}_\mu \rightarrow \bar{\nu}_e$	$\bar{\nu}_e p \rightarrow e + n$	89.5
2	BUB		3664.6
3	DAR $\nu_e$	$\nu_e {}^{12}\text{C} \rightarrow e^- N_{g.s.}$ $\nu_e {}^{12}\text{C} \rightarrow e^- N^*$ $\nu_e {}^{13}\text{C} \rightarrow e^- N$ $\nu e \rightarrow \nu e$	1865.0
4	DIF $\nu_\mu$	$\nu_\mu C \rightarrow \mu^- N^*$ $\nu_\mu C \rightarrow \mu^- N_{g.s.}$	37.3
5	DIF $\bar{\nu}_\mu$	$\bar{\nu}_\mu p \rightarrow \mu^+ n$ $\bar{\nu}_\mu C \rightarrow \mu^+ B^*$ $\bar{\nu}_\mu C \rightarrow \mu^+ B_{g.s.}$	5.9
6	DAR $\bar{\nu}_e$ ( $\mu^-$ DAR)	$\bar{\nu}_e p \rightarrow e^+ n$	16.7
7	$\nu_\mu \rightarrow \nu_e$	$\nu_e C \rightarrow e^- N$	6.1
8	DIF $\pi^+ \rightarrow \nu_e$ and $\mu^+ \rightarrow \nu_e$ decay	$\nu_e C \rightarrow e^- N$	11.9

TABLE XVII: A comparison of the LSND and KARMEN experiments.

Property	LSND	KARMEN
Proton Energy	798 MeV	800 MeV
Proton Intensity	1000 $\mu\text{A}$	200 $\mu\text{A}$
Duty Factor	$6 \times 10^{-2}$	$1 \times 10^{-5}$
Total Mass	167 t	56 t
Neutrino Distance	30 m	17.5 m
Particle Identification	YES	NO
Energy Resolution at 50 MeV	6.6%	1.6%

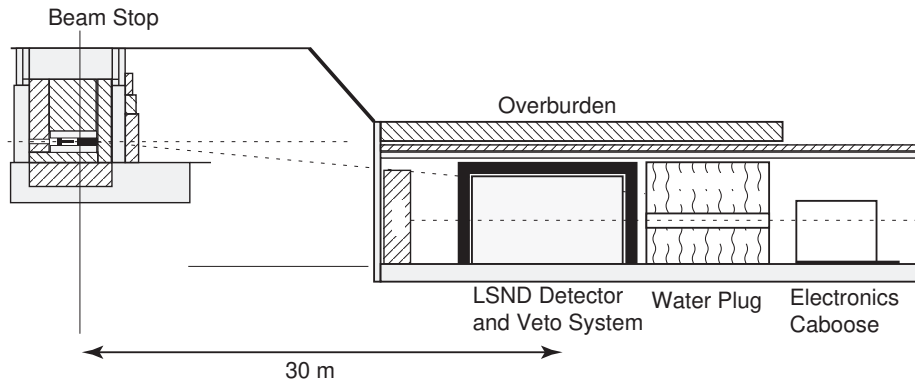


FIG. 1: The layout of the LSND detector and the A6 beam stop area.

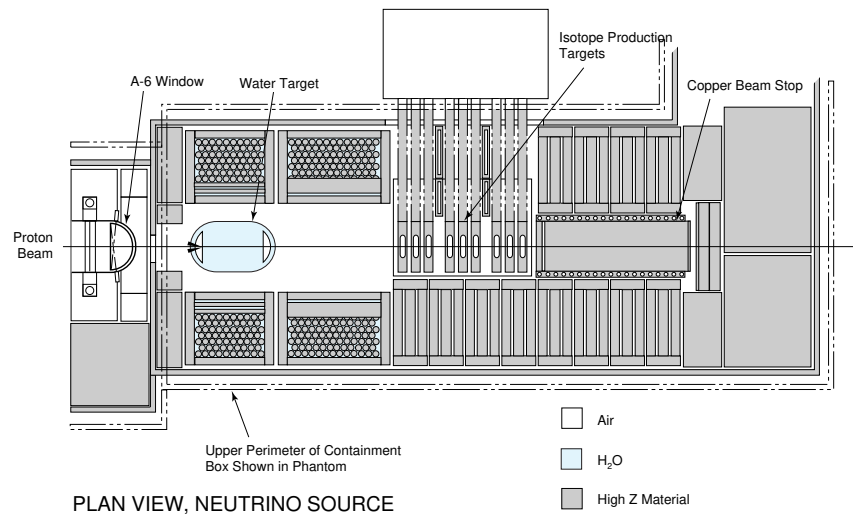


FIG. 2: The layout of the A6 beam stop, as it was configured for the 1993-1995 data taking.



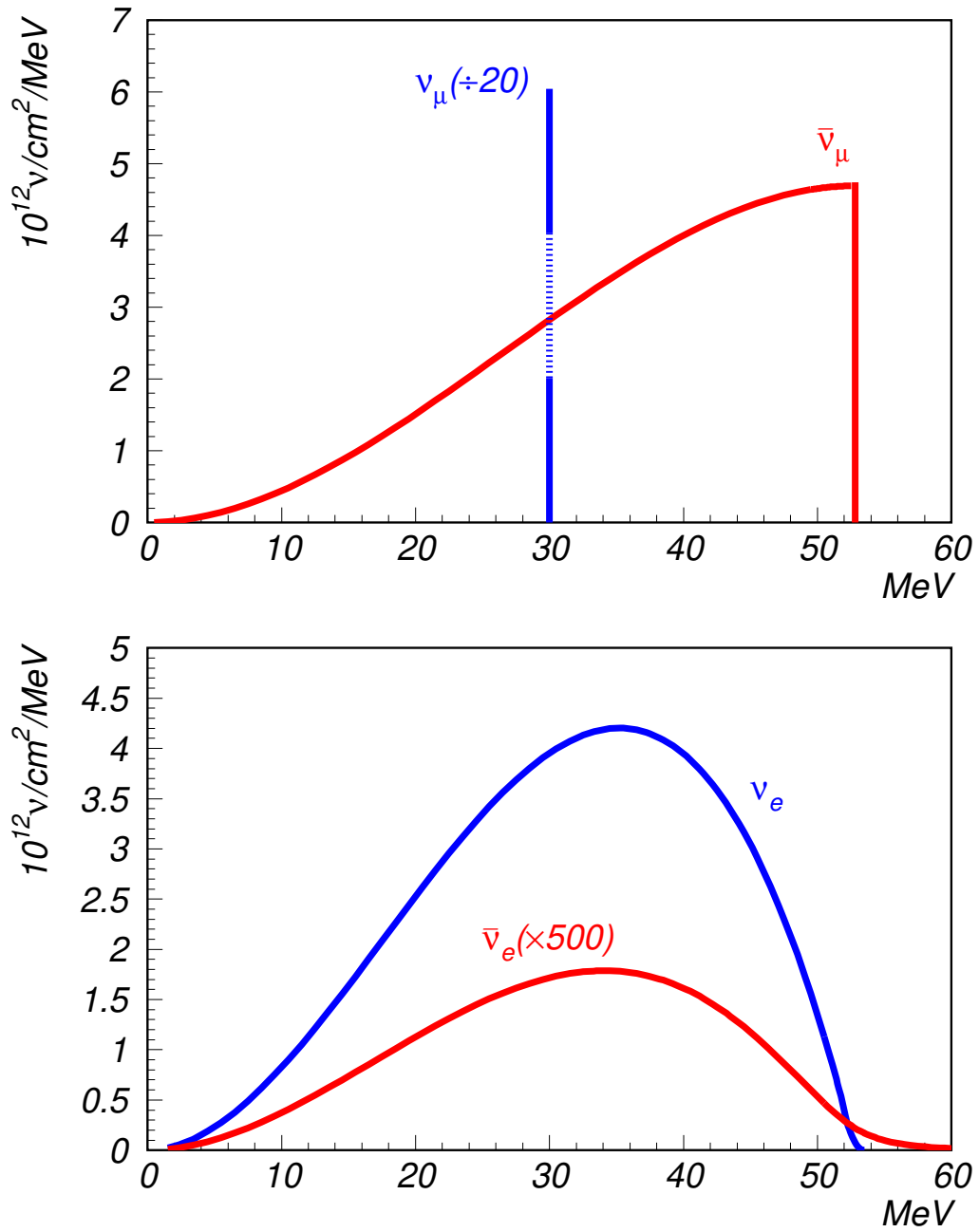


FIG. 3: The decay-at-rest neutrino fluxes averaged over the detector.

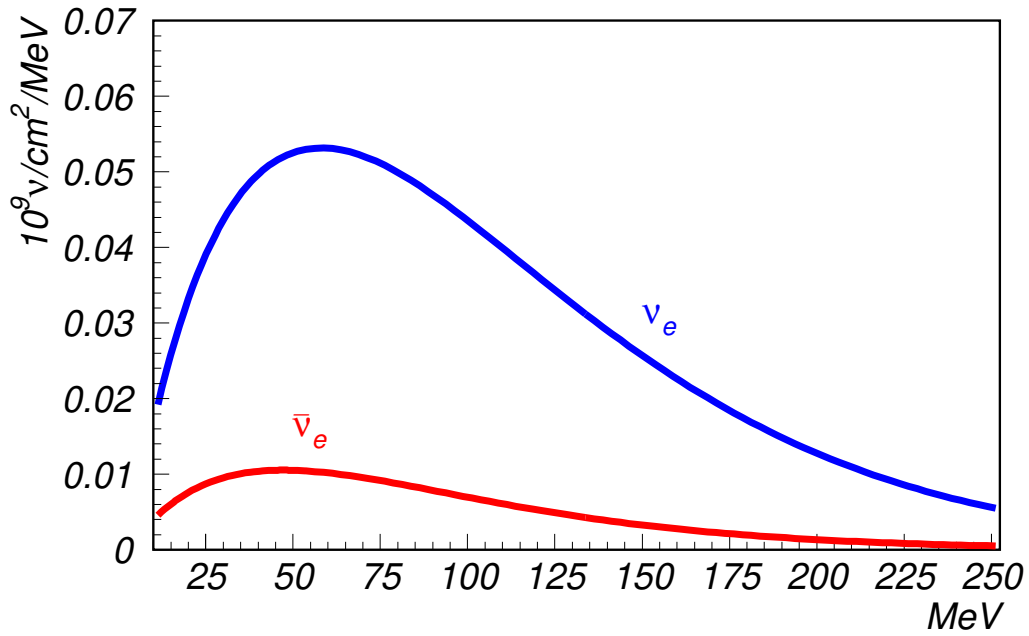
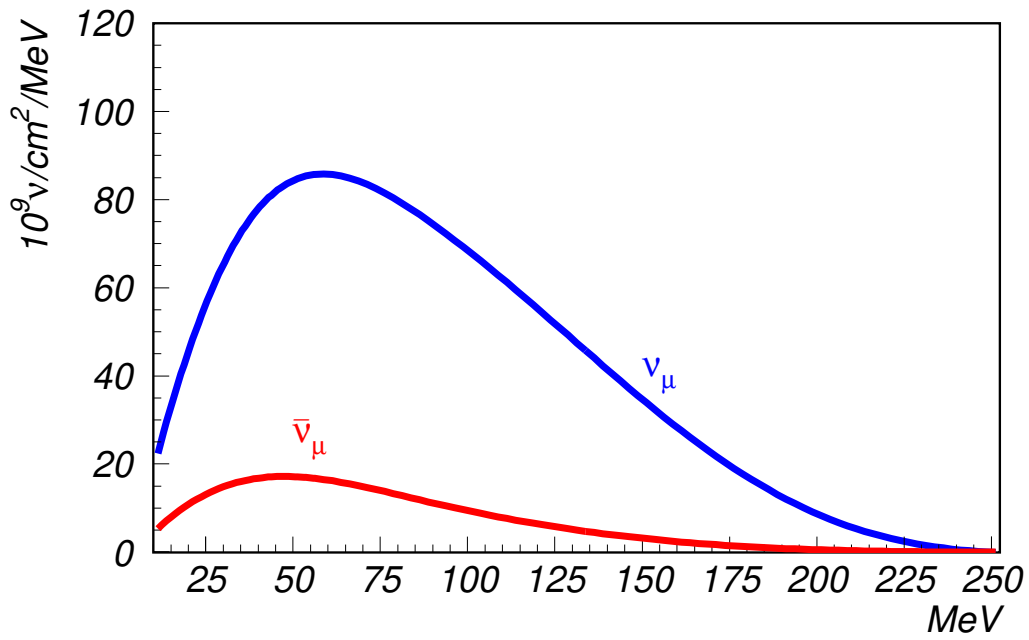


FIG. 4: The decay-in-flight neutrino fluxes averaged over the detector.

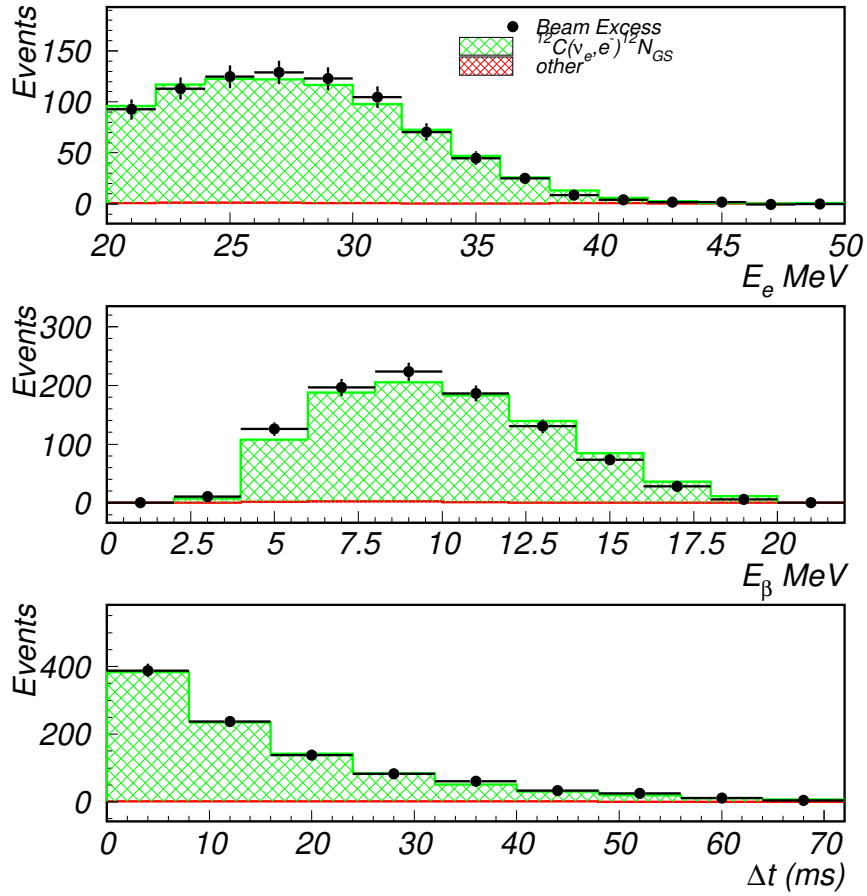


FIG. 5: The electron and  $\beta$  energy distributions and the time between the electron and  $\beta$ ,  $\Delta t$ , for  $^{12}\text{C}(\nu_e, e^-)^{12}\text{N}_{g.s.}$  scattering events.

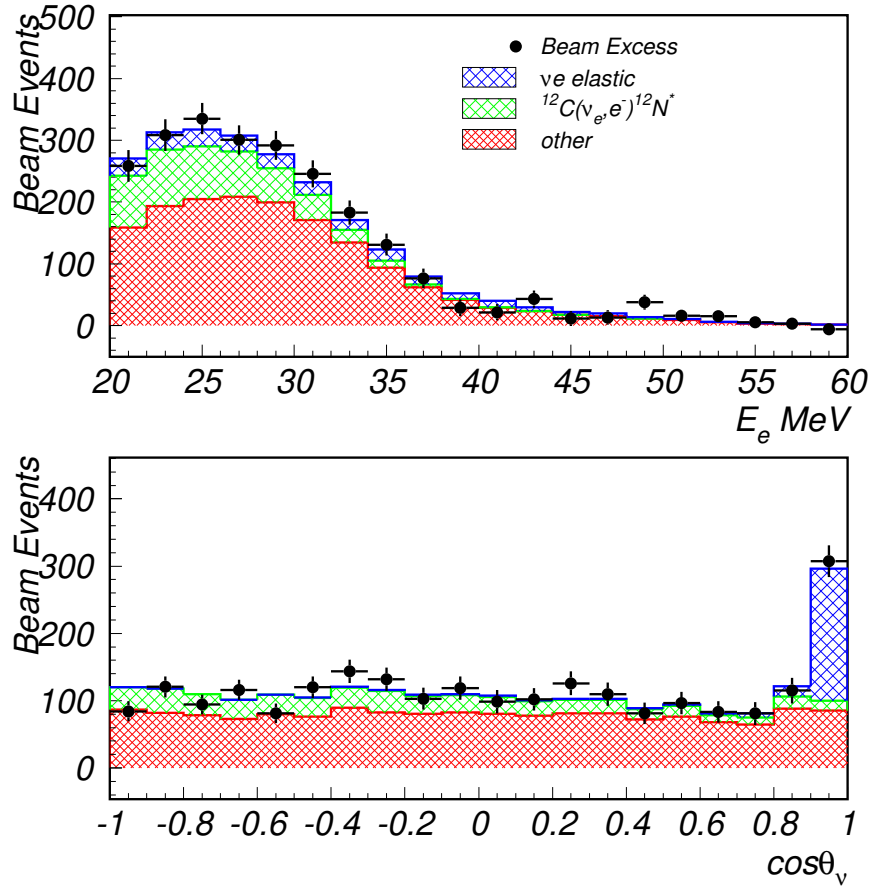


FIG. 6: The energy and angular distributions for inclusive electron events.  $E_e$  is the electron energy and  $\theta_\nu$  is the angle between the incident neutrino and outgoing electron directions. Neutrino-electron elastic scattering events are clearly seen near  $\cos \theta_\nu \sim 1$ .

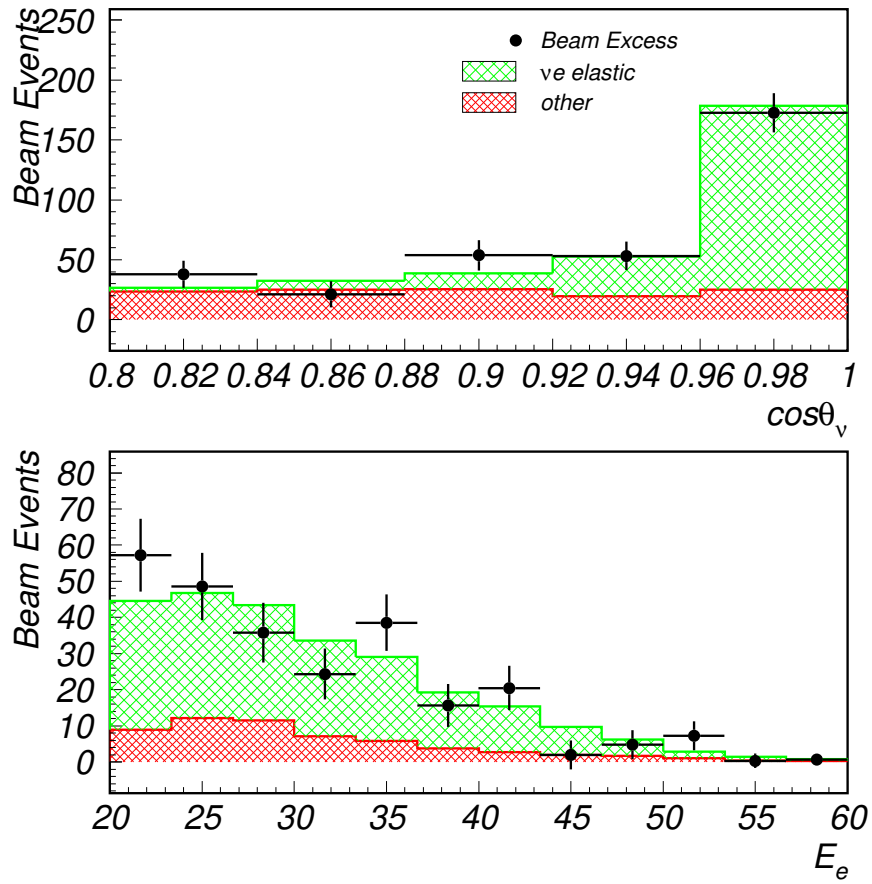


FIG. 7: The angular distribution (top plot) and the energy distribution (bottom plot) for neutrino-electron elastic scattering events with  $\cos \theta_\nu > 0.9$  and with  $^{12}\text{C}(\nu_e, e^-)^{12}\text{N}_{g.s.}$  events removed.

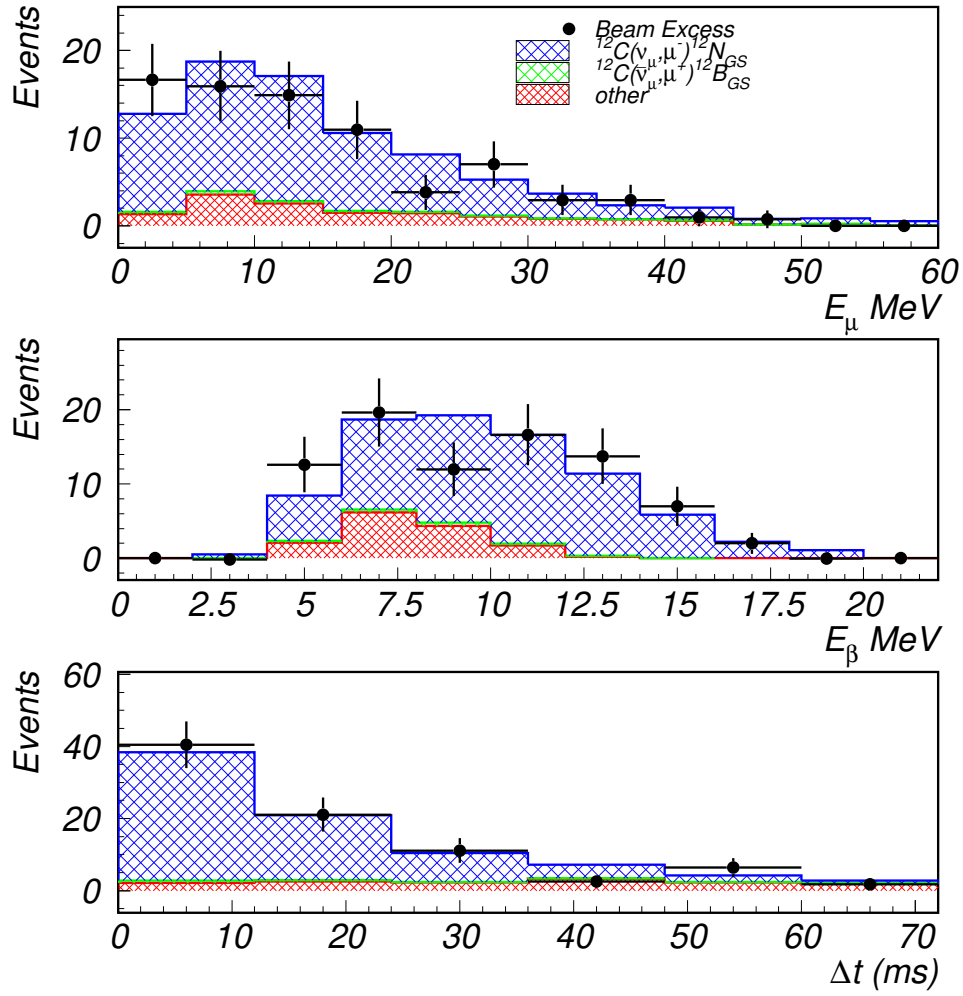


FIG. 8: The muon and  $\beta$  energy distributions (electron energy equivalent) and the time between the muon and  $\beta$  for  $^{12}\text{C}(\nu_\mu, \mu^-)^{12}\text{N}_{g.s.}$  scattering events.

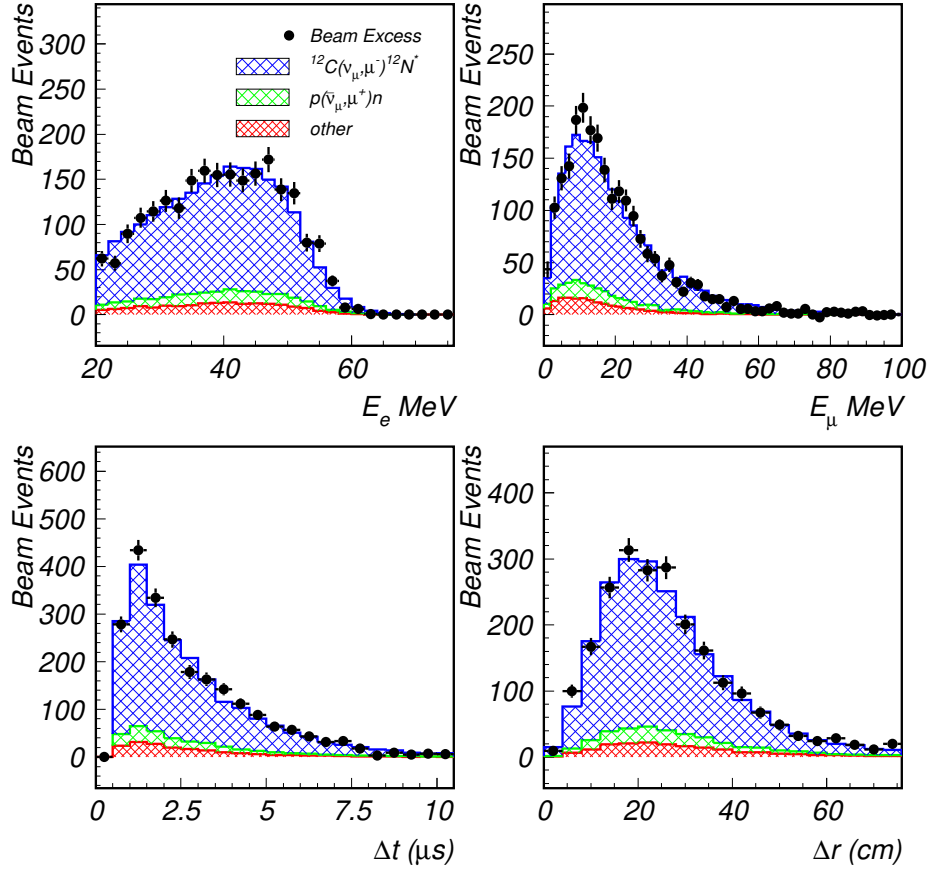


FIG. 9: The Michel electron and muon energy distributions (electron energy equivalent), the time between the muon and electron,  $\Delta t$ , and the distance between the reconstructed electron position and muon position,  $\Delta r$ , for  $\nu_\mu C \rightarrow \mu^- N$ ,  $\bar{\nu}_\mu C \rightarrow \mu^+ B$ , and  $\bar{\nu}_\mu p \rightarrow \mu^+ n$  inclusive scattering events.

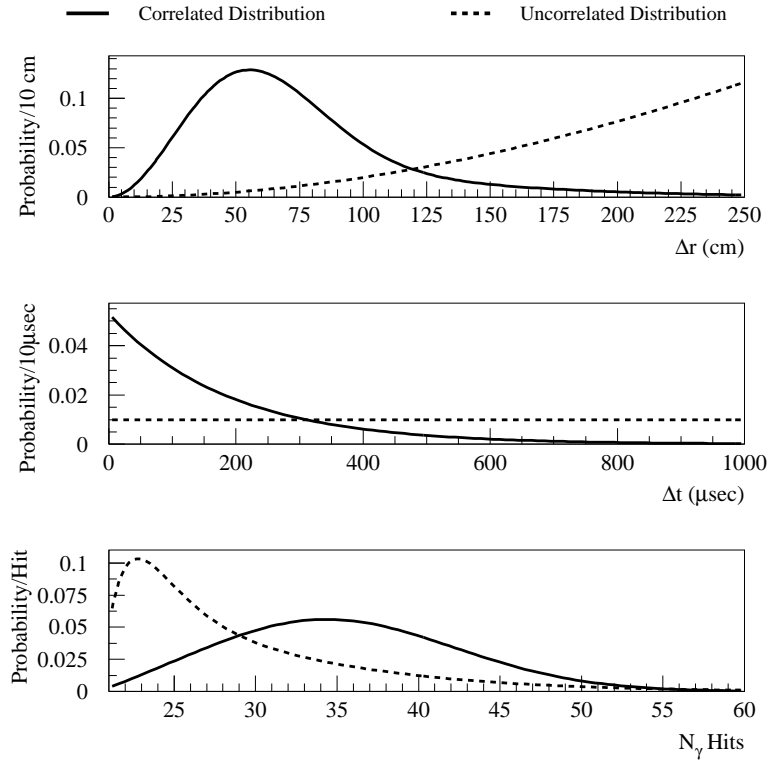


FIG. 10: Distributions for correlated 2.2 MeV  $\gamma$  (solid curves) and accidental  $\gamma$  (dashed curves). The top plot shows the distance between the reconstructed  $\gamma$  position and positron position,  $\Delta r$ , the middle plot shows the time interval between the  $\gamma$  and positron,  $\Delta t$ , and the bottom plot shows the number of hit phototubes associated with the  $\gamma$ ,  $N_{hits}$ .



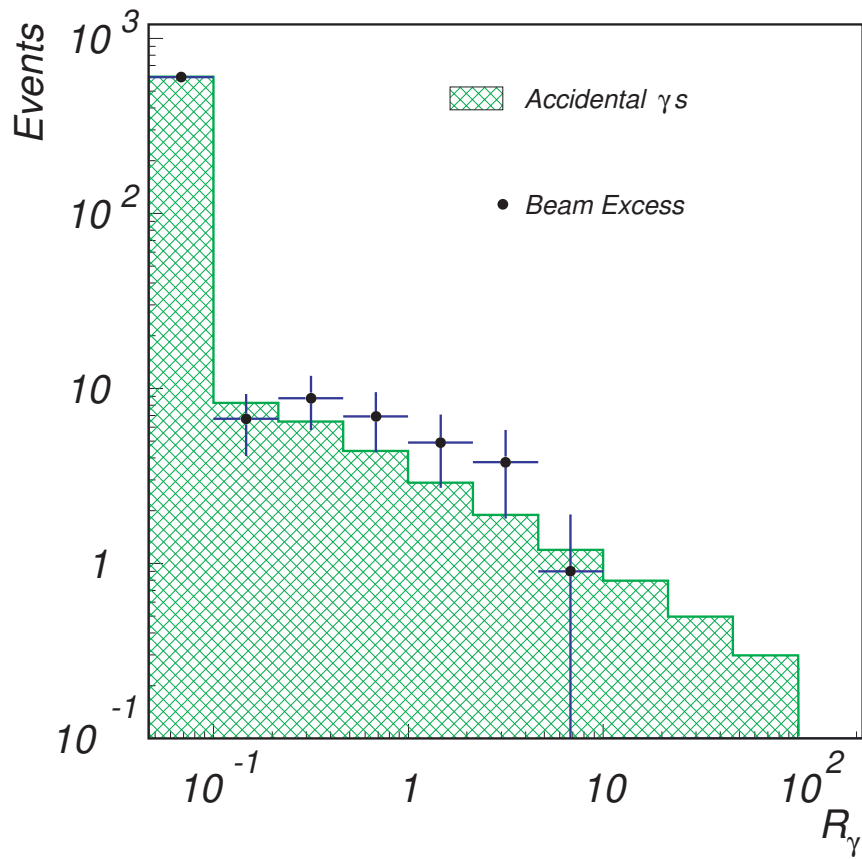


FIG. 11: The  $R_\gamma$  distribution for  $\nu_e C \rightarrow e^- N_{g.s.}$  exclusive events, where the  $N_{g.s.}$   $\beta$  decays. The distribution is consistent with a pure accidental  $\gamma$  shape.

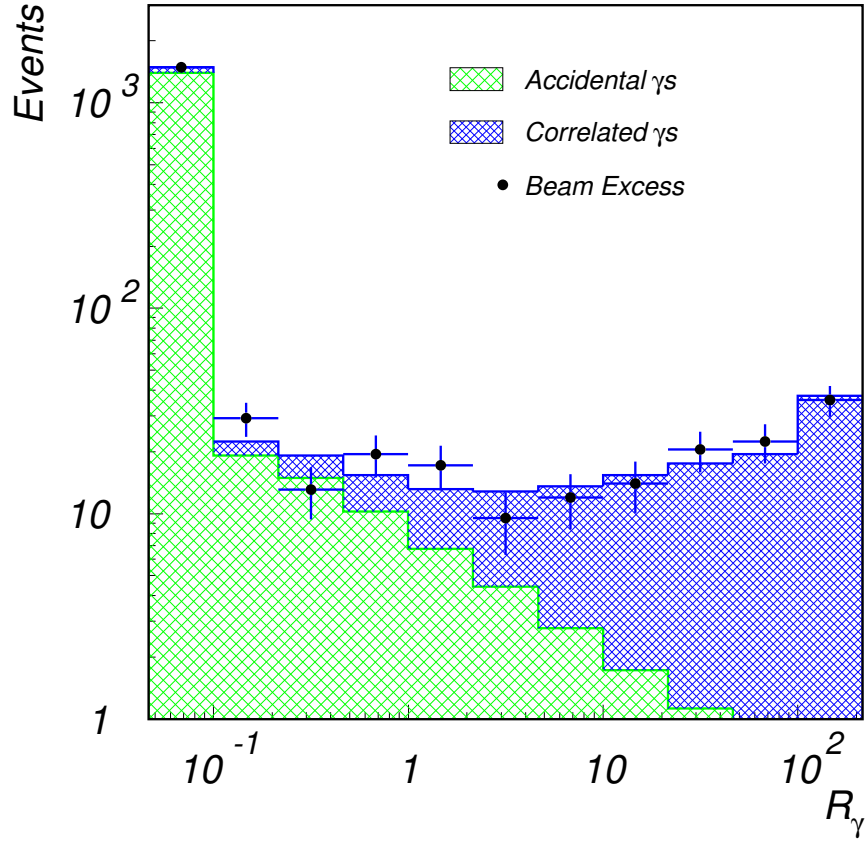


FIG. 12: The  $R_\gamma$  distribution for  $\nu_\mu C \rightarrow \mu^- N$ ,  $\bar{\nu}_\mu C \rightarrow \mu^+ B$ , and  $\bar{\nu}_\mu p \rightarrow \mu^+ n$  inclusive scattering events.

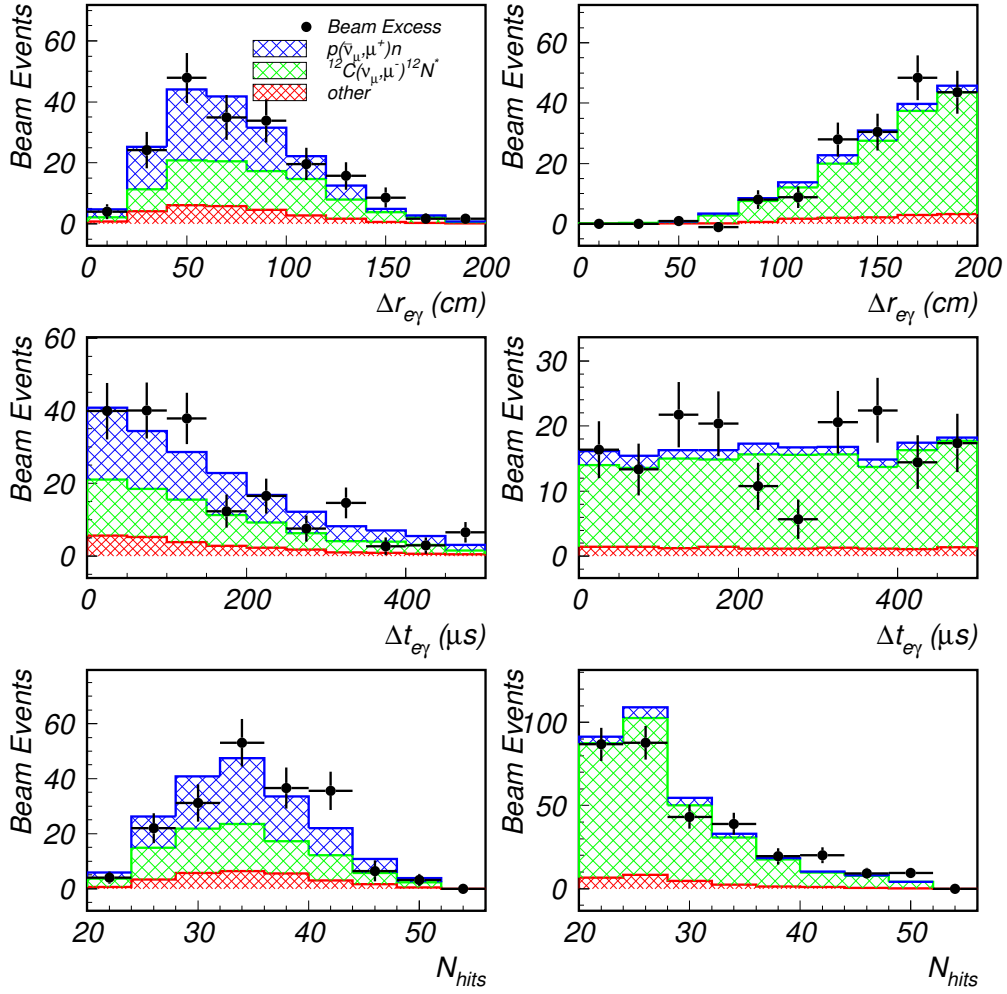


FIG. 13: The individual  $\gamma$  distributions from  $\nu_\mu C \rightarrow \mu^- N$ ,  $\bar{\nu}_\mu C \rightarrow \mu^+ B$ , and  $\bar{\nu}_\mu p \rightarrow \mu^+ n$  scattering for events with  $R_\gamma > 1$  (left side) and  $R_\gamma < 1$  (right side). The top plots show the distance between the reconstructed  $\gamma$  position and positron position,  $\Delta r$ , the middle plots show the time interval between the  $\gamma$  and positron,  $\Delta t$ , and the bottom plots show the number of hit phototubes associated with the  $\gamma$ ,  $N_{hits}$ .

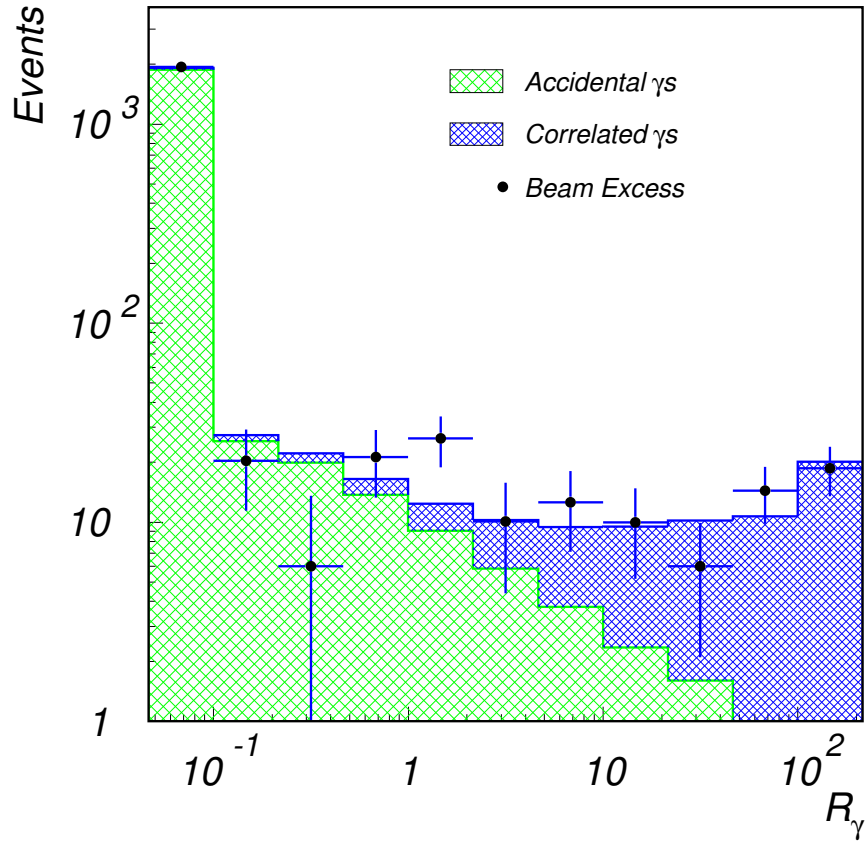


FIG. 14: The  $R_\gamma$  distribution for events that satisfy the selection criteria for the primary  $\bar{\nu}_\mu \rightarrow \bar{\nu}_e$  oscillation search.

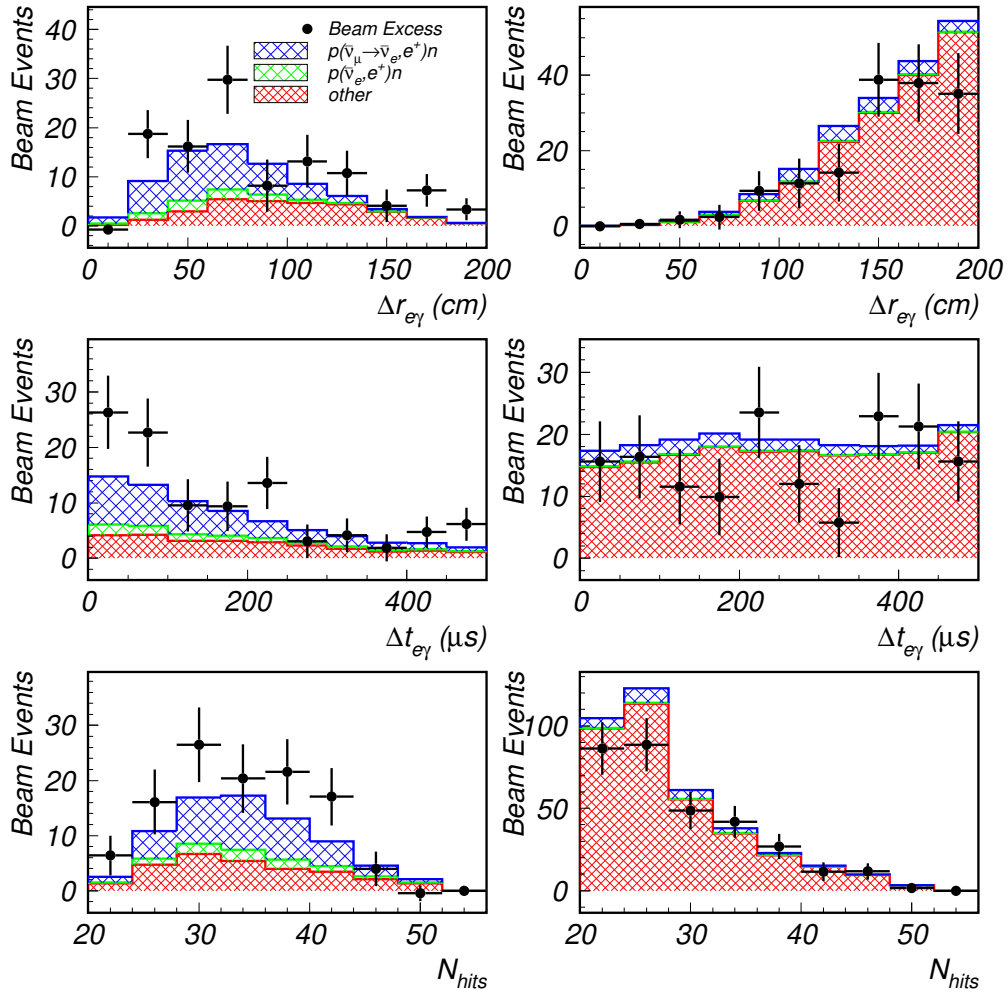


FIG. 15: The individual  $\gamma$  distributions for events that satisfy the selection criteria for the primary  $\bar{\nu}_\mu \rightarrow \bar{\nu}_e$  oscillation search with  $R_\gamma > 1$  (left side) and  $R_\gamma < 1$  (right side). The top plots show the distance between the reconstructed  $\gamma$  position and positron position,  $\Delta r$ , the middle plots show the time interval between the  $\gamma$  and positron,  $\Delta t$ , and the bottom plots show the number of hit phototubes associated with the  $\gamma$ ,  $N_{hits}$ .

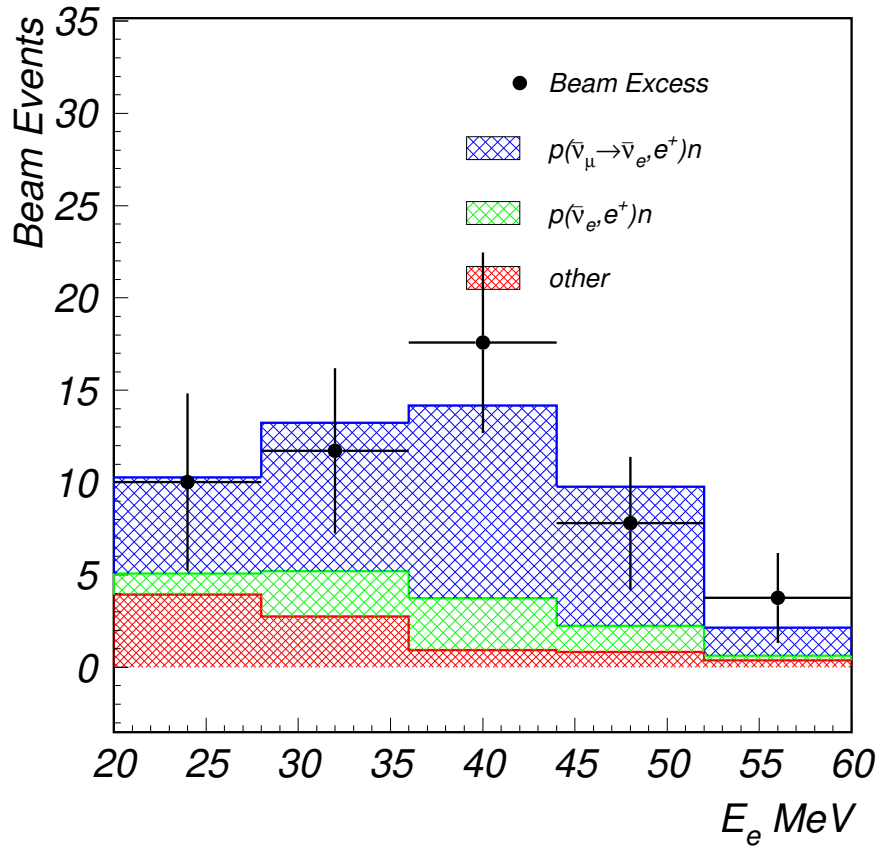


FIG. 16: The energy distribution of the 1993-1998 data sample for events with  $R_\gamma > 10$ . The shaded region shows the expected distribution from a combination of neutrino background plus neutrino oscillations at low  $\Delta m^2$ .

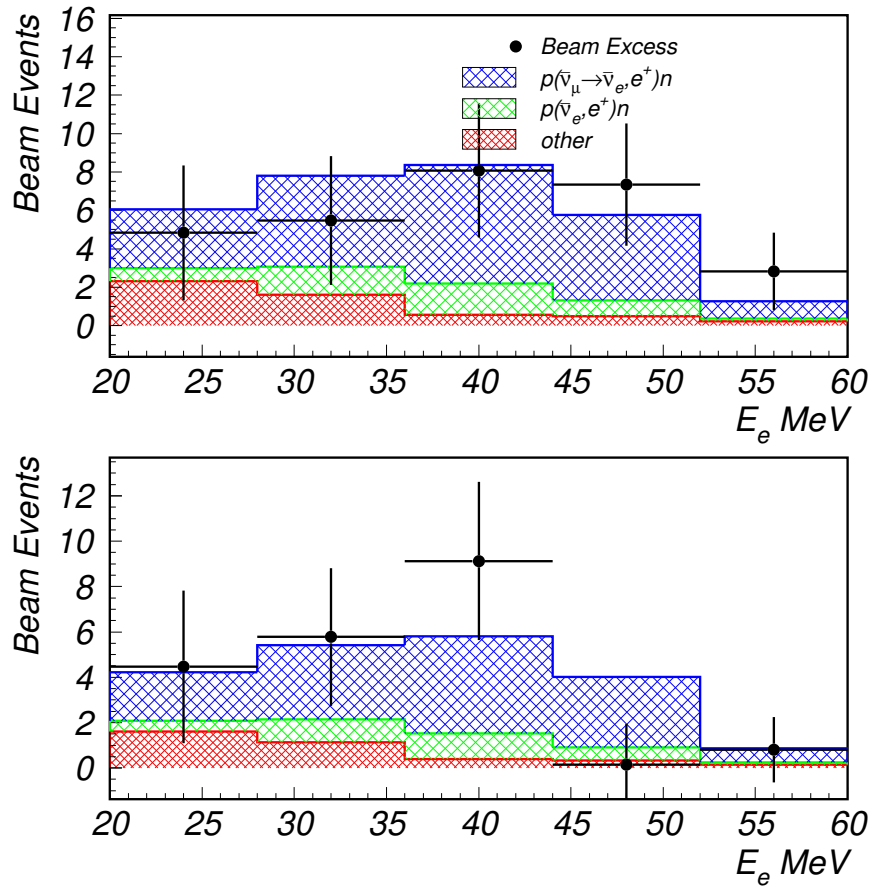


FIG. 17: The energy distribution of the 1993-1995 (top plot) and 1996-1998 (bottom plot) data samples for events with  $R_\gamma > 10$ . The shaded region shows the expected distribution from a combination of neutrino background plus neutrino oscillations at low  $\Delta m^2$ .

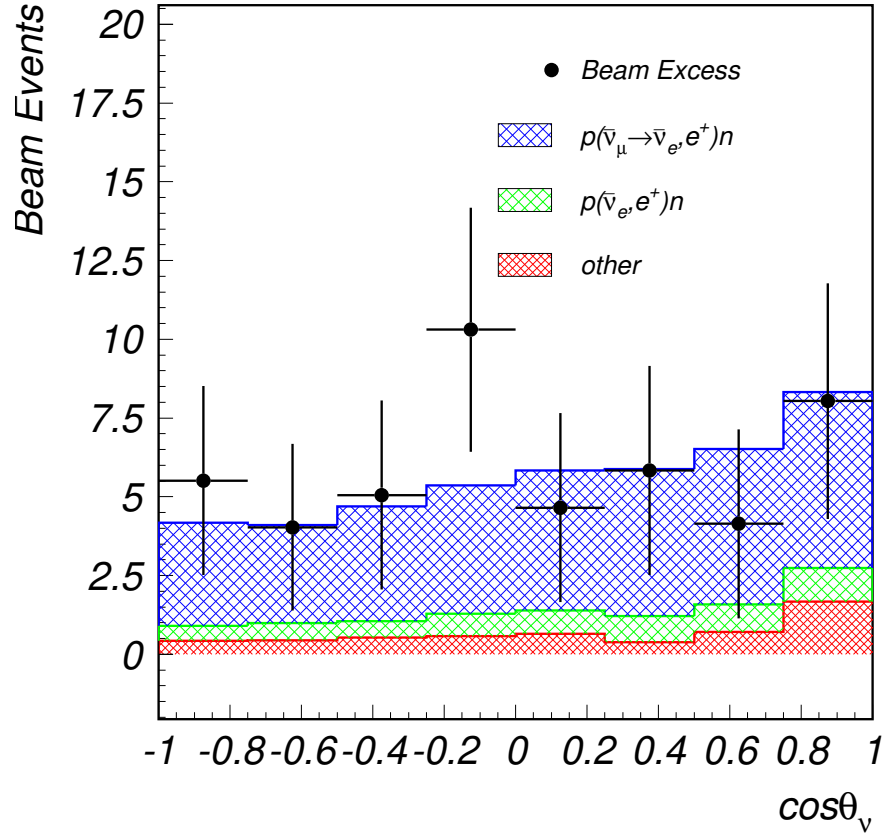


FIG. 18: The  $\cos\theta_\nu$  distribution for events with  $R_\gamma > 1$  and  $36 < E < 60$  MeV. The shaded region shows the expected distribution from a combination of neutrino background plus neutrino oscillations at low  $\Delta m^2$ .



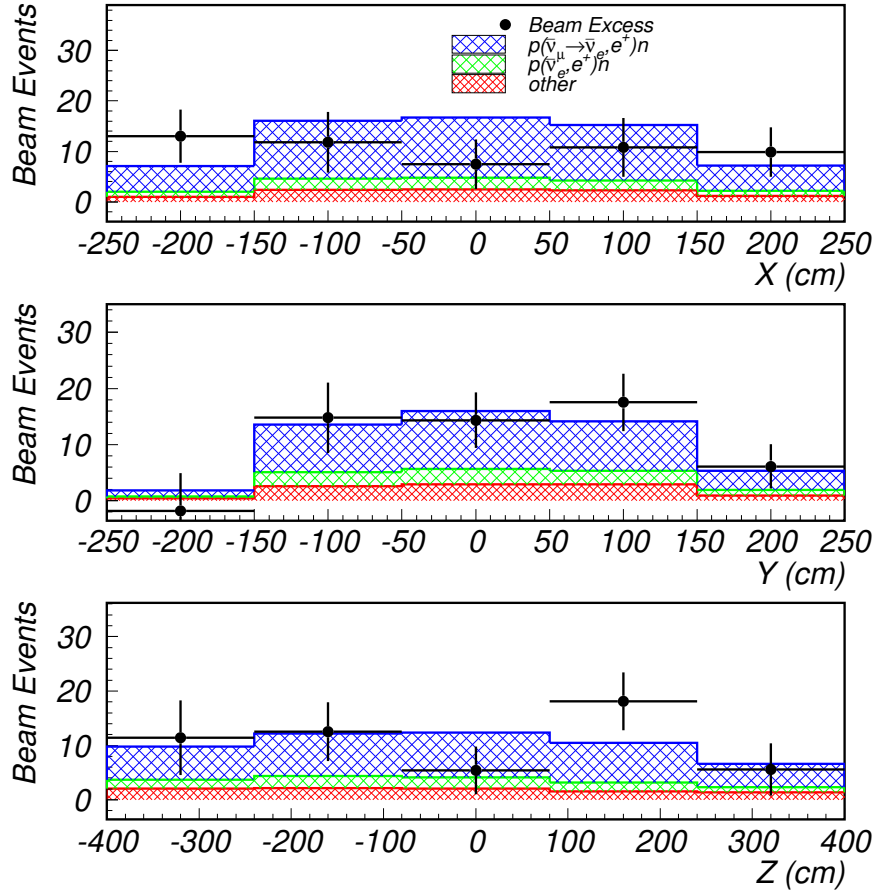


FIG. 19: The spatial distributions for events with  $R_\gamma > 10$ ,  $20 < E_e < 60$  MeV, and  $D > 10$  cm. The shaded region shows the expected distribution from a combination of neutrino background plus neutrino oscillations at low  $\Delta m^2$ .

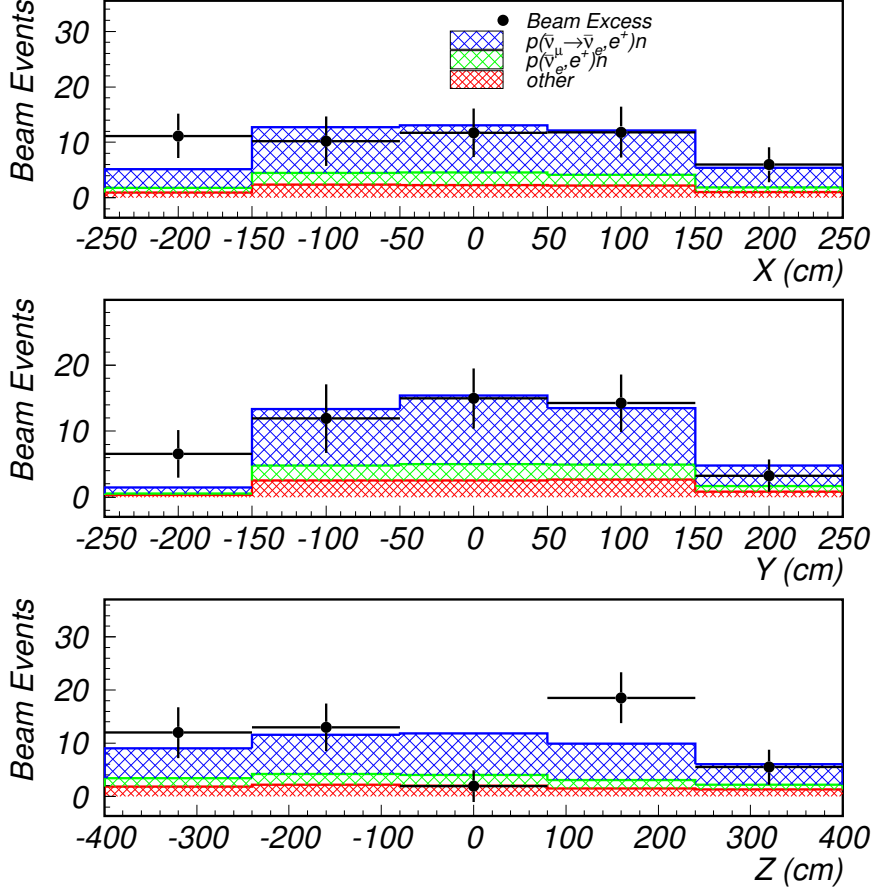


FIG. 20: The spatial distributions for events with  $R_\gamma > 10$ ,  $20 < E_e < 60$  MeV, and  $D > 35$  cm. The shaded region shows the expected distribution from a combination of neutrino background plus neutrino oscillations at low  $\Delta m^2$ .

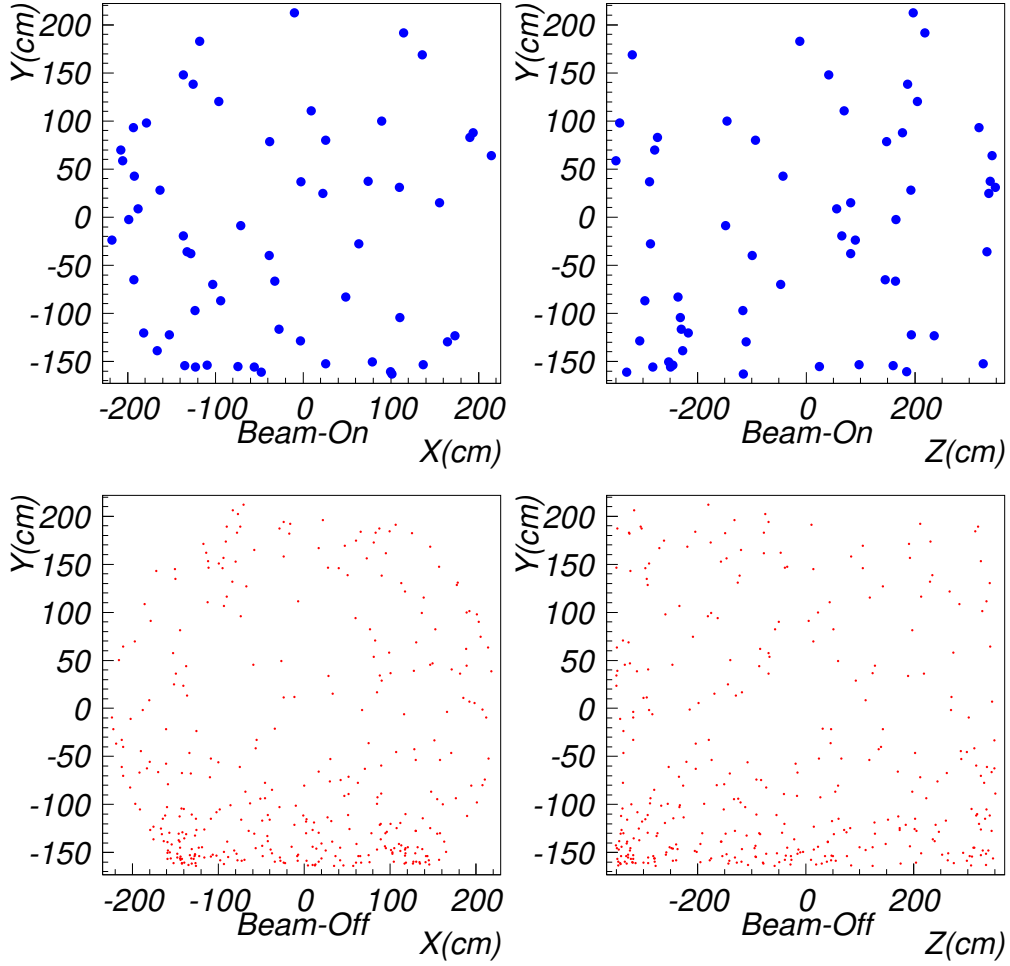


FIG. 21: The scatter plots of the x-y and y-z spatial distributions for events with  $R_\gamma > 10$ ,  $20 < E_e < 60$  MeV, and  $D > 35$  cm. Beam-on and beam-off events are shown separately. The ratio of the dot area in beam-off plots, to the dot area in the beam-on plots, is equal to the duty ratio. This gives the appropriate scale for the beam-off subtraction.

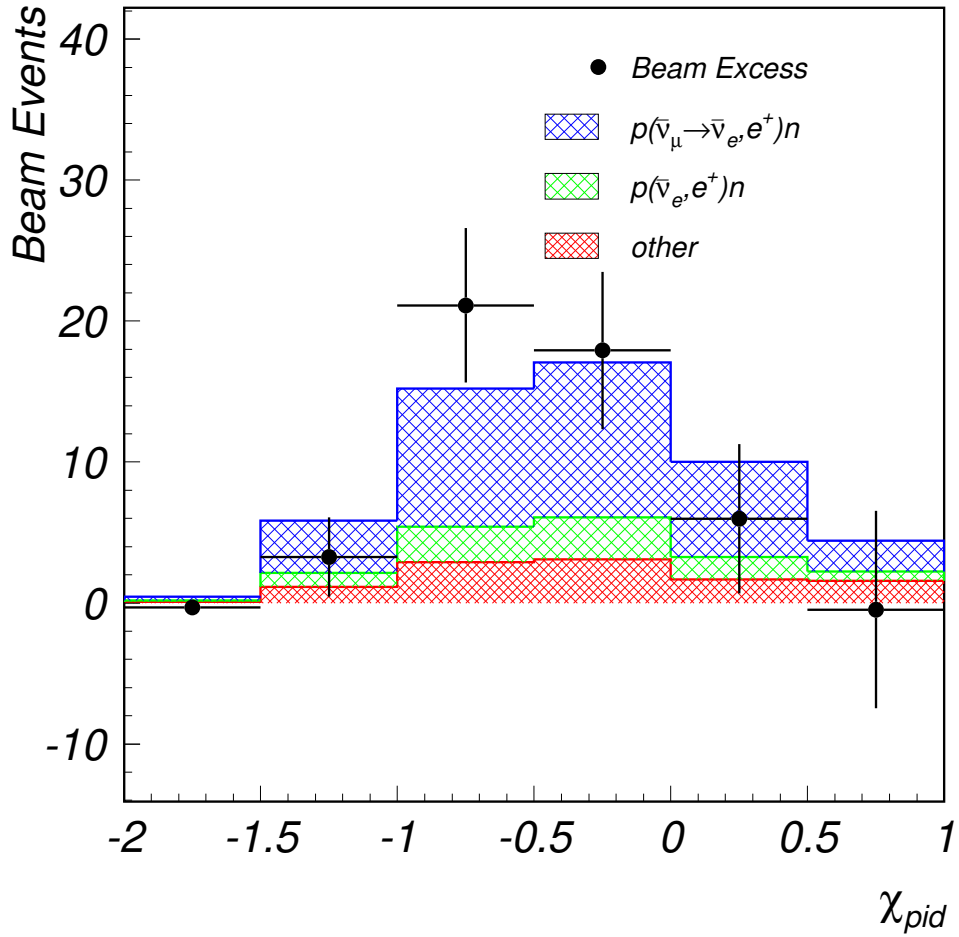


FIG. 22: The particle identification,  $\chi'_{tot}$ , distribution for events with  $R_\gamma > 10$ ,  $20 < E_e < 60$  MeV, and  $D > 35$  cm. The shaded region shows the expected distribution from a combination of neutrino background plus neutrino oscillations at low  $\Delta m^2$ . Oscillation candidate events are required to satisfy the requirement  $-1.5 < \chi'_{tot} < 0.5$ .

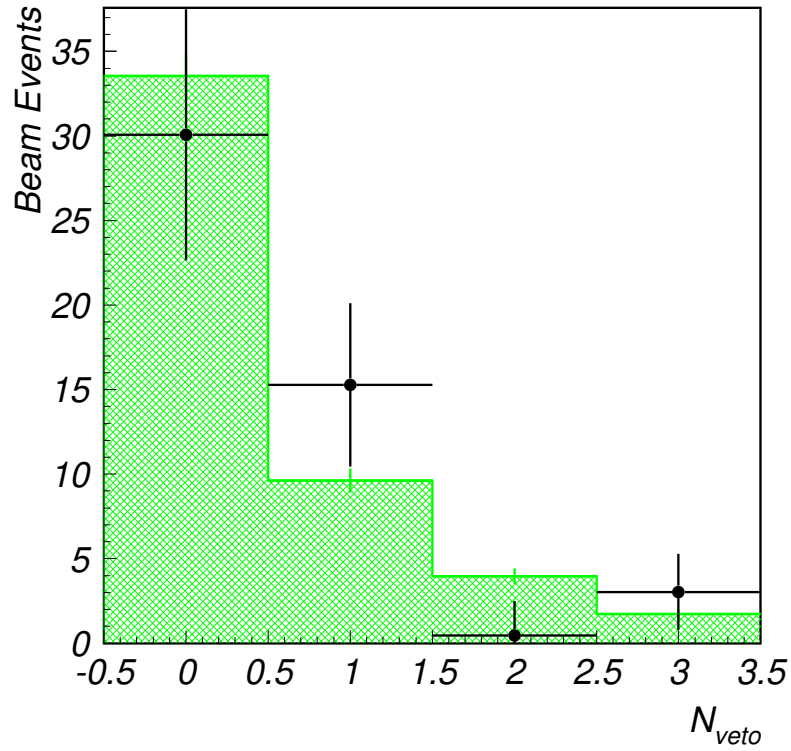


FIG. 23: The veto hit distribution for events with  $R_\gamma > 10$  and  $20 < E_e < 60$  MeV. The data agree well with the distribution from  $\nu_e C \rightarrow e^- N_{g.s.}$  scattering (shaded histogram), where the reaction is identified by the  $N_{g.s.}$   $\beta$  decay.

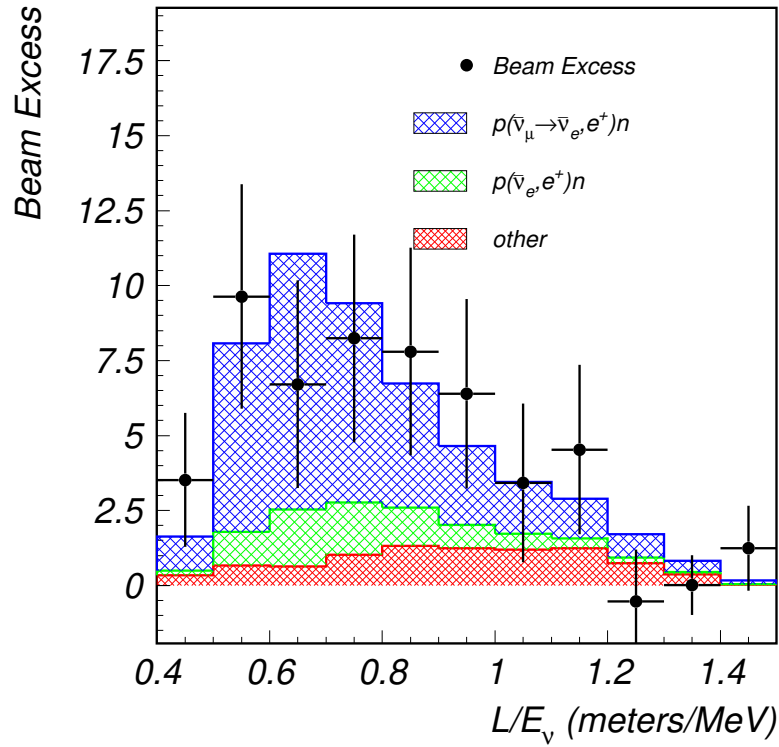


FIG. 24: The  $L_\nu/E_\nu$  distribution for events with  $R_\gamma > 10$  and  $20 < E_e < 60$  MeV, where  $L_\nu$  is the distance travelled by the neutrino in meters and  $E_\nu$  is the neutrino energy in MeV. The data agree well with the expectation from neutrino background and neutrino oscillations at low  $\Delta m^2$ .

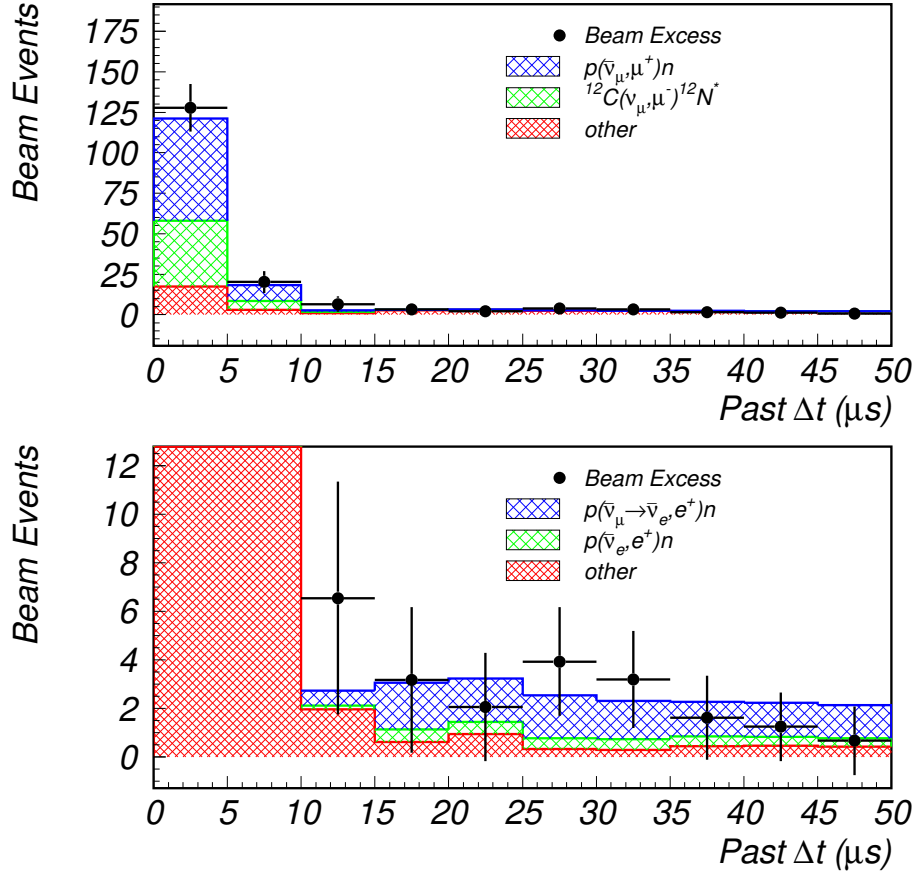


FIG. 25: This figure shows the time to the previous event for  $R_\gamma > 10$  electron events prior to applying the  $\Delta t_{past} > 12\mu\text{s}$  selection. In the upper graph the beam excess events are in agreement with our expectations for  $\bar{\nu}_\mu p \rightarrow \mu^+ n$  and  $^{12}\text{C}(\bar{\nu}_\mu, \mu^+) ^{12}\text{B}^*$  processes. With the same data on a smaller vertical scale, the bottom graph shows events with accidental past activities, in agreement with expectations from random cosmic ray backgrounds and beam related backgrounds. Note that most of the oscillation candidate events have no past activity, and therefore do not appear in these graphs.

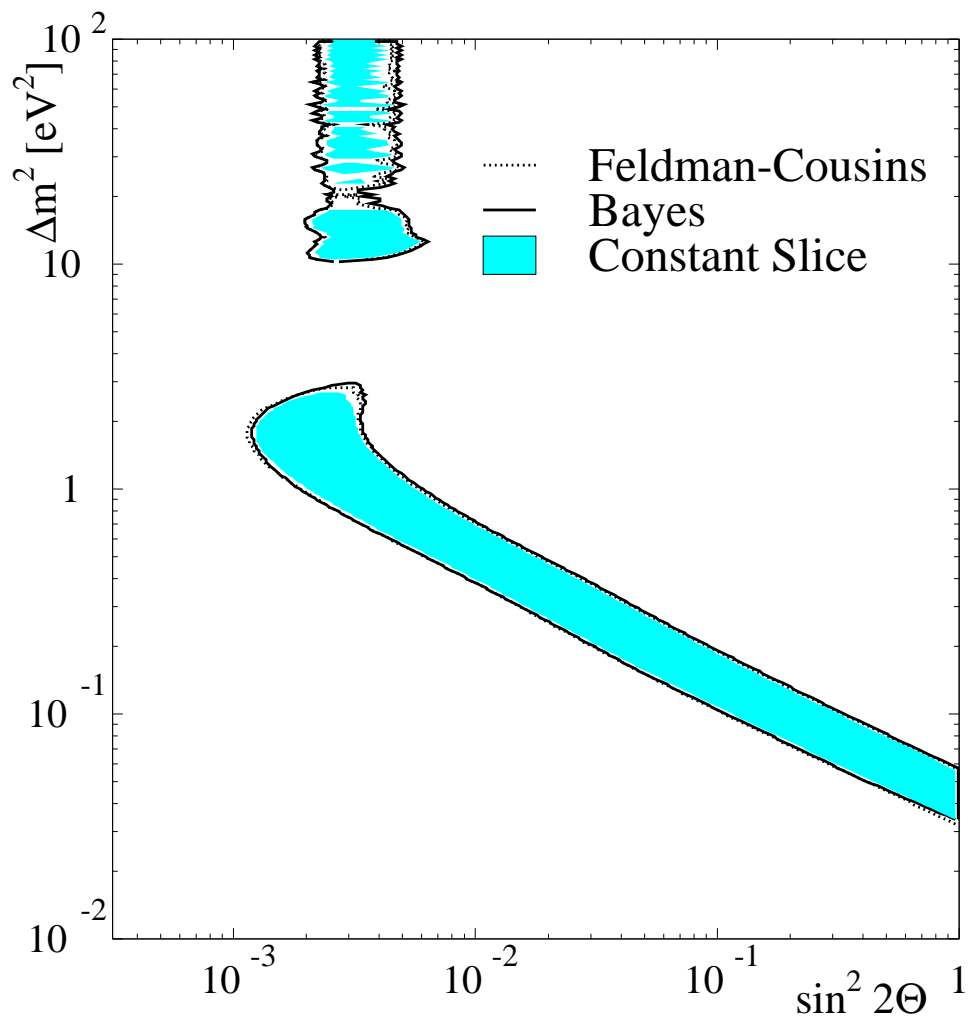


FIG. 26: Favored regions in the  $(\sin^2 2\theta, \Delta m^2)$  plane at 90% CL. The Feldman-Cousins, Bayesian, and constant-slice methods all give about the same result.



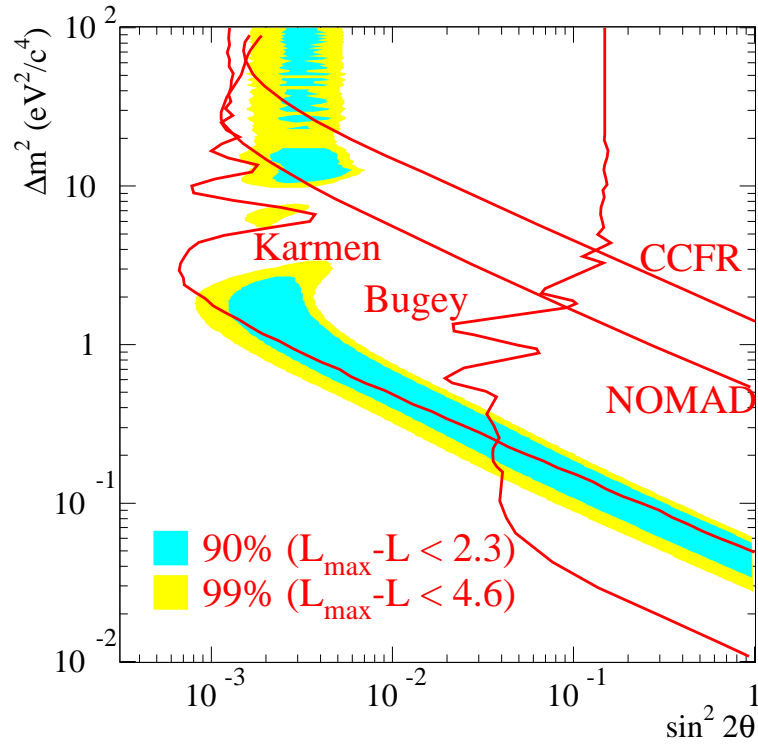


FIG. 27: A  $(\sin^2 2\theta, \Delta m^2)$  oscillation parameter fit for the entire data sample,  $20 < E_e < 200$  MeV. The fit includes primary  $\bar{\nu}_\mu \rightarrow \bar{\nu}_e$  oscillations and secondary  $\nu_\mu \rightarrow \nu_e$  oscillations, as well as all known neutrino backgrounds. The inner and outer regions correspond to 90% and 99% CL allowed regions, while the curves are 90% CL limits from the Bugey reactor experiment, the CCFR experiment at Fermilab, the NOMAD experiment at CERN, and the KARMEN experiment at ISIS.

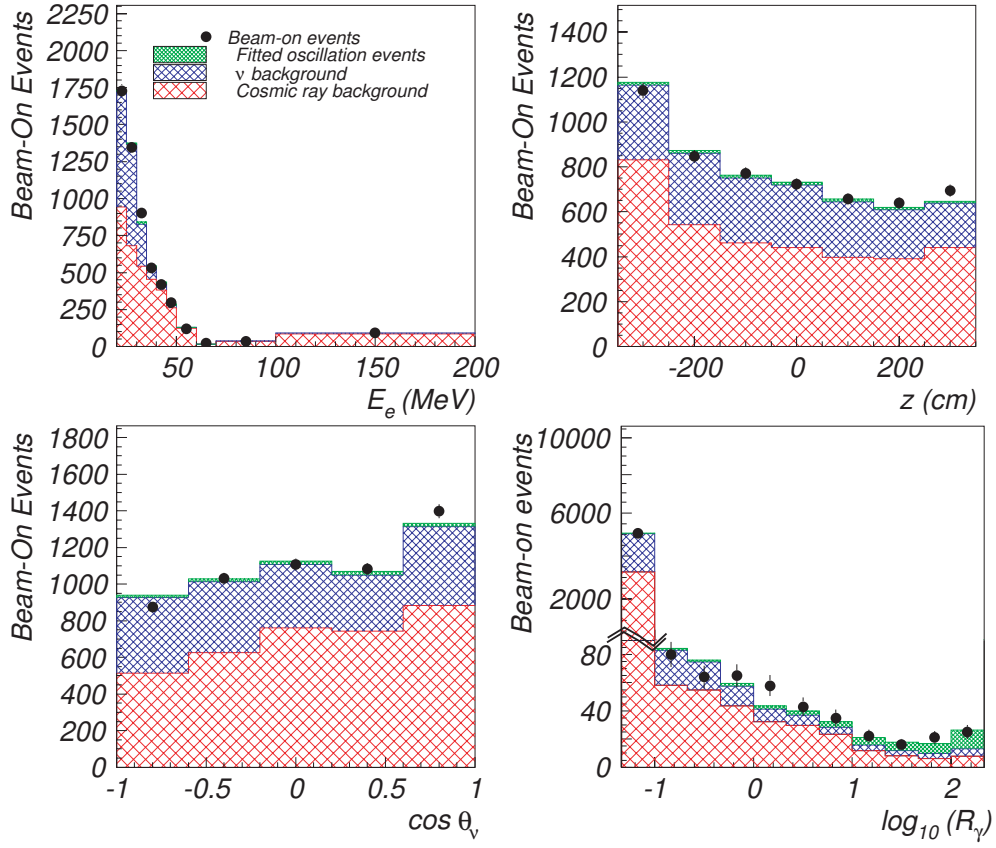


FIG. 28: The  $E_e$ ,  $z$ ,  $\cos \theta_\nu$ , and  $R_\gamma$  projections from the 4-dimensional  $(\sin^2 2\theta, \Delta m^2)$  likelihood fit. The points with error bars are the data.

- 
- [1] C. Athanassopoulos *et al.*, *Phys. Rev. Lett.* **75**, 2650 (1995).
- [2] C. Athanassopoulos *et al.*, *Phys. Rev. C* **54**, 2685 (1996); C. Athanassopoulos *et al.*, *Phys. Rev. Lett.* **77**, 3082 (1996).
- [3] C. Athanassopoulos *et al.*, *Phys. Rev. Lett.* **81**, 1774 (1998); C. Athanassopoulos *et al.*, *Phys. Rev. C* **58**, 2489 (1998).
- [4] For a recent review, see J. N. Bahcall, P. I. Krastev, and A. Yu. Smirnov, *Phys. Rev. D* **58**, 096016 (1998).
- [5] For recent reviews, see G. L. Fogli, E. Lisi, and D. Montanino, *Phys. Rev. D* **49**, 3626 (1994); S. M. Bilenky and C. Giunti, *Phys. Lett. B* **444** 379 (1998).
- [6] Y. Fukuda *et al.*, *Phys. Rev. Lett.* **81**, 1562 (1998); **82**, 2644 (1999); **85**, 3999 (2000).
- [7] D. O. Caldwell and R. N. Mohapatra, *Phys. Rev. D* **48**, 3259 (1993); J. Peltoniemi and J. W. F. Valle, *Nucl. Phys.* **B406**, 409 (1993); S. M. Bilenky, C. Giunti, and W. Grimus, *Prog. Part. Nucl. Phys.* **43**, 1 (1999); V. Barger *et al.*, *Phys. Lett.* **B489**, 345 (2000); T. Goldman, G. J. Stephenson Jr. and B. H. J. McKellar, *Mod. Phys. Lett. A* **15** 439 (2000).
- [8] G. C. McLaughlin, J. M. Fetter, A. B. Balantekin, and G. M. Fuller, *Phys. Rev. C* **59**, 2873 (1999); D. O. Caldwell, G. M. Fuller, and Y.-Z. Qian, *Phys. Rev. D* **61**, 123005 (2000).
- [9] C. Athanassopoulos *et al.*, *Nucl. Instrum. Methods A* **388**, 149 (1997).
- [10] R. L. Burman, M. E. Potter, and E. S. Smith, *Nucl. Instrum. Methods A* **291**, 621 (1990); R. L. Burman, A. C. Dodd, and P. Plischke, *Nucl. Instrum. Methods in Phys. Research A* **368**, 416 (1996).
- [11] S. N. Nakamura *et al.*, *Phys. Rev. A* **45**, 6202 (1992).
- [12] T. Suzuki, D. F. Measday, J. P. Roalsvig, *Phys. Rev. C* **35**, 2212 (1987).
- [13] R. A. Reeder *et al.*, *Nucl. Instrum. Methods A* **334**, 353 (1993).
- [14] J. J. Napolitano *et al.*, *Nucl. Instrum. Methods A* **274**, 152 (1989).
- [15] A. C. Hayes and I. S. Towner, *Phys. Rev. C* **61**, 044603 (2000).
- [16] E. Kolbe, K. Langanke, and S. Krewald, *Phys. Rev. C* **49**, 1122 (1994); E. Kolbe, K. Langanke, and P. Vogel, *Nucl. Phys.* **A652**, 91 (1999).
- [17] GEANT3.21, a CERN detector description and simulation tool, CERN program library long writeup W5013.

- [18] E. J. Moniz, *Phys. Rev.* **184**, 1154 (1969).
- [19] R. A. Smith and E. J. Moniz, *Nucl. Phys.* **B43**, 605 (1972).
- [20] C. Athanassopoulos *et al.*, *Phys. Rev. C* **55**, 2078 (1997).
- [21] C. Athanassopoulos *et al.*, *Phys. Rev. C* **56**, 2806 (1997).
- [22] L. B. Auerbach *et al.*, to be published in *Phys. Rev. D*.
- [23] L. B. Auerbach *et al.*, to be submitted to *Phys. Rev. C*.
- [24] L. B. Auerbach *et al.*, to be submitted to *Phys. Rev. C*.
- [25] C. H. Llewellyn Smith, *Physics Reports* **3**, 262 (1972); P. Vogel, *Phys. Rev. D* **29**, 1918 (1984);  
P. Vogel and J. F. Beacom, *Phys. Rev. D* **60**, 053003 (1999).
- [26] M. Fukugita, Y. Kohyama, and K. Kubodera, *Phys. Lett. B* **212**, 139 (1988).
- [27] E. Kolbe, K. Langanke, F.-K. Thielmann, and P. Vogel, *Phys. Rev. C* **52**, 3437 (1995).
- [28] This background also includes contributions from  $\bar{\nu}_\mu C \rightarrow \mu^+ n X$  and  $\nu_\mu C \rightarrow \mu^- n X$ .
- [29] K. Eitel, *New Jour. Phys.* 2:1 (2000).
- [30] G. J. Feldman and R. D. Cousins, *Phys. Rev. D* **57**, 3873 (1998).
- [31] B. Achkar *et al.*, *Nucl. Phys.* **B434**, 503 (1995).
- [32] A. Romosan *et al.*, *Phys. Rev. Lett.* **78**, 2912 (1997).
- [33] D. Autiero, talk presented at the 1998 International Conference on High Energy Physics in Vancouver, Canada.
- [34] K. Eitel, talk presented at the 2000 International Neutrino Conference in Sudbury, Canada.
- [35] E. Church *et al.*, "A proposal for an experiment to measure  $\nu_\mu \rightarrow \nu_e$  oscillations and  $\nu_\mu$  disappearance at the Fermilab Booster: BooNE", LA-UR-98-352, Fermilab experiment 898.